

Assembly Processes for Scintillator Planes in the MINER ν A Neutrino Detector

A thesis submitted in partial fulfillment of the requirement
for the degree of Bachelor of Science with Honors in
Physics from the College of William and Mary in Virginia,

by

Kelly E. Sassin

Accepted for _____
(Honors)

Advisor: Dr. Jeffrey Nelson

Dr. Gina Hoatson

Dr. Gunter Luepke

Williamsburg, Virginia
May 2007

Abstract

This research project involves the MINER ν A neutrino detector, a high statistics neutrino scattering experiment being built to run in the NuMI neutrino beamline at the Fermi National Accelerator Laboratory. MINER ν A is a hexagonal shaped detector that will be placed in the beamline directly upstream of the MINOS near detector at Fermilab, and it is designed to study neutrino-nucleus interactions. MINER ν A will increase the precision of the MINOS neutrino oscillation by reducing systematic errors in the mass splitting measurement, and it will allow for precision neutrino interaction measurements. The core of the hexagonal detector is made up of 30,000 segmented plastic scintillation counters. In this research project we developed a set of prototypes of the optical readout for the MINER ν A scintillator planes. We tested them mechanically and optimized the optical design. We developed production tests that optimized the scintillator planes to be light-tight, durable, able to maintain tight alignment tolerances, and without optical faults. This project also included studies to optimize the testing of the initial scintillator production assemblies for uniformity and position resolution using radioactive sources and cosmic ray muons.

Acknowledgments

I would first like to thank my advisor Professor Jeff Nelson for making this research possible through his help and encouragement throughout the year. I would also like to thank Dan Damiani for his invaluable help with coding and his willingness to help and answer my questions. I would also like to thank the rest of the professors that I have had in class that have helped guide me throughout my college career. I would also like to thank my Mom for all of her love and support throughout my college career. Lastly I wish to thank the Honors Committee for taking the time to evaluate my research.

Contents

Abstract	iv
1 Introduction	1
2 MINERνA	3
2.1 Scintillators and PMTs	5
3 MINERνA versus MINOS	6
4 Building the MINERνA Inner Detector Planes	8
4.1 Gluing the Plane	9
4.2 Fiber Routing and Optical Adhesive	10
5 Outer Detector Scintillator	13
5.1 Results	16
6 Monte Carlo Simulation	23
6.1 Radioactive Decay	23
6.2 Energy Loss and Range of Beta Particles	24
6.3 Absorption of Gamma Rays	25
6.4 Compton scattering	25
7 Mapsim	27
7.1 Geometry	28
7.2 Data	29
7.3 Results	31
8 Conclusions	41
8.1 Construction	41
8.2 Monte Carlo Simulation	42

References	44
Appendices	45
A Monte Carlo Geometry Construction	45
B OD testing code	52

List of Figures

1	Front view of the MINER ν A detector in front of MINOS.	4
2	diagram of how the triangular strips are placed to form an array.	6
3	Diagram of the MINER ν A Inner Detector planes: showing the 127 scintillator strips, fiber routing, and PVC combs and edge pieces.	7
4	The weaving of the Lexan material through the array of triangular scintillator. The picture above shows a representation of how the Lexan relates to the ID scintillator strips, while the picture below shows the Lexan actually weaved through the whole plane. This picture does not show the top Lexan skins.	8
5	Diagram of the finished plane including fibers routed onto the Canvex sheets. The plane only needs to have the fibers placed in optical connectors and have a second piece of Canvex sheeting placed over the fibers in order to make them light tight. . .	10
6	The figure on the left shows the Lexan wrapped outer detector scintillator pair. The figure on the right shows a diagram of the top OD strip with its slot in the top and the fiber role.	13
7	Fiber Routing of one OD scintillator tower. A set of 4 OD doublets is routed into a single connector.	14
8	Diagram of WLS fibers inside the fiber holes of the ID or OD scintillator. On the left is a picture of a fiber without optical epoxy, while on the right is a picture of a WLS fiber optically coupled to the scintillator with epoxy	14
9	Diagram of the setup for testing the for OD pairs. The diagram shows the test setup for one of the OD doublets. The triggers are placed on top of the doublet, while the WLS fibers are routed through the doublet and also read into a PMT [6].	16

10	The different distributions between the gaussian and averaged mean. The blue line represents the gaussian mean, while the yellow line represents the calculated average. The data plot of the integrated charge measured in PicoCoulombs versus the length of the scintillator with length 1356.4 in Figure 10. It shows the differences between the calculated and averaged mean.	17
11	The plots represent the gaussian fits of the data peak and the pedestal taken at the 30 cm point on and OD doublet that has had its top and ends painted and its fiber glued into its slot. The graph on the right ia a zoomed version of the graph on the left.	18
12	Pedestal leading edge interfering with gaussian fit of data. The data peak and the pedestal are very close together so the left edge of the pedestal is interfering with the fit of the data peak. (The pedestal can be seen rising on the right hand side of the plot).	19
13	Results of outer detector strip testing with a calculated mean. Along the x -axis are the positions triggered on each of the OD doublets. Along the y -axis is the charge collected by the PMT measured in nanoCoulombs.	21
14	Results of outer detector strip testing with the gaussian average. Along the x -axis are the positions triggered on each of the OD doublets. Along the y -axis is the charge collected by the PMT measured in nanoCoulombs. This graph shows much more uniform curves than the plot of the gaussian mean of each of the data peaks.	22
15	Ionizing Action of Incident Electron [12]	24
16	Volume Geometry of the MapSim Monte Carlo Simulation. The graph on the right represents the initial configuration, while the graph on the left represents a 180° flip of the plane in the x direction.	28
17	The figure on the right shows the zinc encased source without the thin layer of iron to absorb the electrons produced by the decay of the ^{137}Cs . The figure on the left is a zoomed version of the right hand side picture showing slight penetration of the electrons into the scintillator.	29

18	1 event in the <i>Mapsim</i> Monte Carlo simulation.	30
19	Neutrino dominated simulation. This figure shows an unfiltered visualization of 100 events.	31
20	Energy deposition of the electrons produced in the decay of ^{137}Cs	32
21	Distribution of 10^6 events over 21 scintillators strips. Strip 10 is a 0° oriented strip directly over the source	33
22	Depiction of a plot of the current measured in nanoAmps predicted by the Monte Carlo simulation as a function of the scintillators position with respect to the ^{137}Cs source. The red curve represents the current expected from a bottom scintillator strip, while the blue curve represents the current expected in a top scintillator strip.	34
23	Example geometry for the ^{90}Sr source, which also shows 10^3 radioactive decays.	35
24	Energy distribution of electrons produced in the decay of ^{90}Sr . The graph represents the energy of every beta particle produced in 10^5 events.	36
25	Geometry for the simulation of Sr90, this figure also shows 10^3 radioactive decay events.	37
26	Depiction of a plot of the current measured in nA predicted by the Monte Carlo simulation as a function of the scintillators position with respect to the ^{90}Sr source. The red curve represents the current expected from a bottom scintillator strip, while the blue curve represents the current expected in a top scintillator strip.	38
27	Energy distribution of electrons produced in the decay of ^{106}Ru . The graph represents the energy of every beta particle produced in 10^5 events.	40

1 Introduction

The neutrino was first postulated by Wolfgang Pauli in 1930 to explain conservation of energy in beta decay. Pauli theorized that an undetected particle was carrying away the observed difference between the energy and momentum of the initial and final particles. However, the first experimental detection of neutrinos did not come until 1956, when Clyde Cowan, Frederick Reines, F. B. Harrison, H. W. Kruse, and A. D. McGuire discovered the electron neutrino produced in beta decay from a nuclear reactor.

Later experiments determined that there were three types, or flavors of neutrinos, corresponding to the known charge carrying leptons: the muon μ , the electron e , and the tau τ , which gives each of the three neutrinos their names: the electron neutrino ν_e , the muon neutrino ν_μ , and the tau neutrino ν_τ . Because the neutrino is an electrically neutral lepton, it does not interact by way of the strong electromagnetic forces, but only through the weak force and gravity. Because the cross section in weak nuclear interactions is very small, neutrinos can pass through matter almost unhindered. [1]

Although the neutrino interacts very infrequently, researchers have discovered two types of neutrino interactions: charged current and neutral current. In charged-current interactions the neutrino transforms into its partner lepton due to an exchange of a W boson. However, there is an energy threshold to these interactions, and if the neutrino does not have sufficient energy to produce its partner lepton, then the neutrino cannot interact via charged-current interactions. Along with the charged lepton (e , μ , τ) some of the initial neutrino's energy is transferred to the nucleus. This recoiling system represents the debris of the struck nucleon in the nucleus of the target atom. In a CC interaction the neutrino's energy converted to "visible" energy in the form of the resulting particles. In a neutral current interaction, the neutrino leaves the detector after having transferred some of its energy and momentum to a

target particle. All three neutrino flavors can participate regardless of the neutrino energy. However, no neutrino flavor information is left behind. [3]

Neutrinos, because we can “see” them from the charged lepton produced in their interactions, are most often created or detected with a well defined flavor (electron, muon, tau). However, in a phenomenon known as neutrino flavor oscillation, neutrinos are able to oscillate between the three available flavors while they propagate through space. Specifically, this occurs because the neutrino flavor eigenstates are not the same as the neutrino mass eigenstates, whose propagation can be described by plane wave solutions of the form:

$$|\nu_i(t)\rangle = e^{-i(E_i t - \vec{p}_i \cdot \vec{x})} |\nu_i(0)\rangle \quad (1)$$

Where E_i is the energy of the mass-eigenstate i , t is the time from the start of the propagation, \vec{p}_i is the 3-dimensional momentum, \vec{x} is the current position of the particle relative to its starting position. If we take the ultrarelativistic limit, where the momentum is much greater than the mass, an approximation we can make since mass approximations of neutrino are less than 1 eV, the wavefunction can be written as:

$$|\nu_i(L)\rangle = e^{-im_i^2 L/2E} |\nu_i(0)\rangle \quad (2)$$

Where L represents the distance traveled and m_i represents the masses of the different neutrinos. Eigenstates with different masses propagate at different speeds. The heavier ones lag behind while the lighter ones pull ahead. Since the mass eigenstates are combinations of flavor eigenstates, this difference in speed causes interference between the corresponding flavor components of each mass eigenstate. Constructive interference causes it to be possible to observe a neutrino created with a given flavor to change its flavor during its propagation. The probability that a neutrino originally of flavor μ will later be observed as having flavor τ can be written in the following

form:

$$P(\nu_\mu \rightarrow \nu_t; t) = |\langle \nu_\tau | \nu_\mu(t) \rangle|^2 \quad (3)$$

Condensing this equation down to a two neutrino admixture we get:

$$P(\nu_\mu \rightarrow \nu_t; t) = \sin^2(2\theta) \sin^2(1.27 \Delta m^2 L/E) \quad (4)$$

Where $\sin^2(2\theta)$ parameterizes the mixing angle and $\Delta m^2 = m_\tau^2 - m_\mu^2$. [14] The wavelength of the oscillations depends on the energy, E , of the neutrinos. Therefore a crucial ingredient in any neutrino oscillation analysis is the determination of the neutrino's energy. Both the MINOS and MINER ν A experiments aim to produce precision measurements of the neutrino mass squared difference (Δm) and mixing angle (θ) of neutrino oscillations. [3]

2 MINER ν A

The MINOS neutrino oscillation experiment studies neutrino interactions occurring in the 2 to 10 GeV region using a much coarser detector than MINER ν A is expected to be, producing less detailed knowledge of each interaction. Figure 1 shows a schematic of the MINER ν A upstream of the MINOS near detector. The goal in MINOS is to measure the energy of the incoming neutrinos by summing all energy deposited in the detector in an interaction through the calorimetric method. In calorimetry, a composite detector using the total absorption of particle measures the energy and position of incident particles. In the process of absorption showers are generated by cascades of interactions, where characteristic interactions with matter, i.e. ionization, of the incident particles are used to generate detectable effects. These limitations mean that the MINOS detector cannot, for example, see individual particles and the overall neutrino energy measurement is inferred from particle yield information from

prior experiments. The energy seen in the detector is largely proportional to the momentum of the produced particles and not sensitive to their rest masses. Poor knowledge of the particles produced in neutrino-nucleus interactions in this energy range leads to systematic errors on the neutrino energy determination in MINOS.

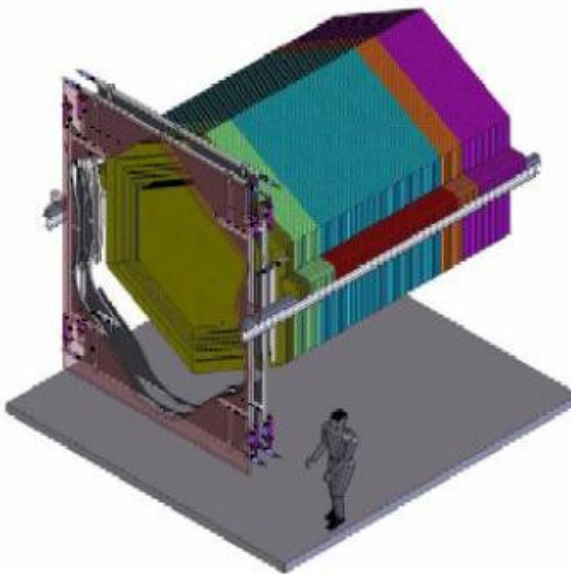


Figure 1: Front view of the MINERνA detector in front of MINOS.

We understand neutrino interactions at higher energies with protons and very light nuclei but more study needs to be done on massive nuclei, in which some of the particles produced in the interactions are scattered or absorbed by other nucleons before they escape the nucleus and effect the visible energy and angle seen from the interaction. In MINOS these interactions are on iron. The high Z of the iron nucleus introduces new complications in the neutrino energy calculations. The struck nucleon will not be at rest but will have some zero point energy, commonly referred to as the Fermi energy. Studies of the number and types of particles produced in neutrino-nucleus interactions with the MINERνA detector will increase the precision of the MINOS energy determination and reduce systematic errors in the measured delta mass squared interval. The MINERνA detector contains a variety of nucleons,

including He, C, Fe, Pb to look at the effects versus Z of the target.

The hexagonally shaped MINER ν A detector will be composed of a totally active Inner Detector (ID), constructed entirely of 196 hexagonal arrays of scintillation counters. The Outer Detector (OD) portion of the hexagon will be composed of six trapezoids of steel (towers) and scintillator acting as a sampling calorimeter, where the energy deposited is proportional to the amount of light produced.

2.1 Scintillators and PMTs

The MINER ν A scintillator is made of polystyrene doped with blue-emitting fluorescent compounds. Both the scintillator that makes up the Outer Detector (OD) as well as the Inner Detector (ID) scintillator, consist of extruded polystyrene coated with a TiO₂ outer layer for reflectivity, and a hole through the middle for a wavelength shifting (WLS) fiber. As charged particles travel through the scintillator, electrons are ionized. As these electrons return to their ground state, they release a photon of blue light that travels through the scintillator impacting the embedded fiber, transforming the blue photon isotropically into a green photon. The collected green photons pass down the length of the fiber where they strike a photomultiplier tube (PMT).

The number of photoelectrons per minimum ionizing particle (MIP) was extrapolated from another Monte Carlo Simulation called LITEYLDX. It was originally written by Keith Ruddick and Jeffrey Nelson and modified for the MINER ν A detector's triangular extruded scintillator. They then input the average light yield from the MINOS scintillator, which was already known to be 4.25 PE at 4 meters. They then calculated the attenuation of the fibers with the equation:

$$N(x) = Ae^{-x/0.9m} + e^{-x/7.0m} \quad (5)$$

They discovered that for particle identification, as well as coordinate resolution and

vector tracking the triangular scintillator used in MINER ν A requires 13.2 PE per layer per minimum ionization particle (MIP) at normal incidence for the full fiber readout.[4]

3 MINER ν A versus MINOS

In MINOS when the detectors were assembled, the direction of the scintillator strips in each layer (or plane) was alternated. A particle passing through the detector only hit one scintillator per layer of scintillators yielding a significant uncertainty in the actual location where the particle traversed the scintillator. MINER ν A, however, is being designed to provide a more detailed and accurate position determination and to improve our ability to resolve the trajectory of multiple particles coming from a neutrino interaction. One of the ways that MINER ν A is designed to accomplish this greater position is with nested triangular scintillator strips as shown in Figure 2.

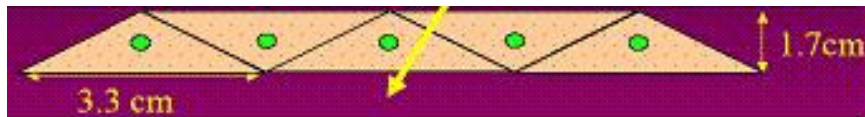


Figure 2: diagram of how the triangular strips are placed to form an array.

Each triangular strip has a base of 3.3cm and a height of 1.7cm. Using this triangular array, the location of the event can be found with significantly improved position resolution. As a charged particle passes through the array (see the arrow in Figure 2) it strikes two scintillating triangles. As this occurs, light that is emitted from the ionization of the electrons in the polystyrene goes to both fibers (one in each of the triangles). This action is called light sharing. Based on the ratio of the light output read from each of these strips, the exact trajectory of the particle can be determined with improved precision. Another way in which MINER ν A will increase

the precision of its measurements is that the scintillator planes are orientated in three directions (x , u , and v directions). These are orientated at 0° , 60° , and -60° . This arrangement helps solve ambiguities when more than one particle passes through the same plane. Figure 3 shows a diagram of the entire inner detector plane, including the 127 scintillator strips with the fibers routed through the top.

With these modifications to the shape and orientation of the scintillator, MINER ν A

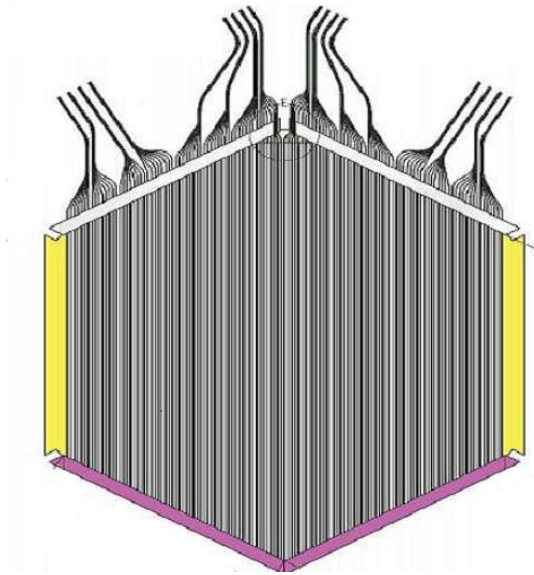


Figure 3: Diagram of the MINER ν A Inner Detector planes: showing the 127 scintillator strips, fiber routing, and PVC combs and edge pieces.

will be able to track more than one particle at a time, as well as determine their angle with good resolution in the inner detector. We can obtain the particles energy by calorimetry, and we can determine their range in the inner detector, because the length of the trajectory is roughly proportional to the particles energy. Or since the MINOS detector is directly downstream of MINER ν A, the MINOS near detector can be used through calorimetry to detect the range of particles as well. With a small fine grained detector we will be able to get samples of neutrino interactions that are 100 or in some cases 1000 times larger than previous samples.

4 Building the MINER ν A Inner Detector Planes

This year we made the first fully instrumented prototype planes. Plane 1 was assembled in the fall semester, and Plane 2 was constructed over winter break. The real assembly of the MINER ν A planes will begin this summer. Each inner detector scintillator plane is constructed of 127 triangular scintillator pieces collectively wrapped in Lexan, a polycarbonate, light-tight, fire retardant material which will keep the light produced in an interaction contained to its plane. When the strips arrive they are in thirteen foot long strips, so must first be cut to fit the hexagonal shape of the plane.

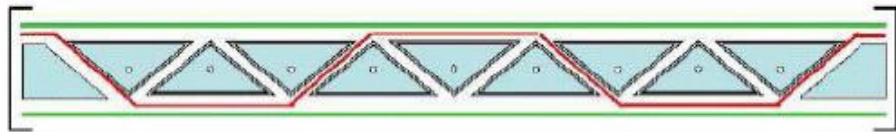


Figure 4: The weaving of the Lexan material through the array of triangular scintillator. The picture above shows a representation of how the Lexan relates to the ID scintillator strips, while the picture below shows the Lexan actually weaved through the whole plane. This picture does not show the top Lexan skins.

After the strips have been cut and cleaned, the strips are placed on the plane preparation table, which is made out of melamine laminate to ensure vacuum sealing, where we assemble and build the plane. Since there are 127 scintillator strips in the inner detector plane and each strip will be moved periodically throughout the construction, the strips are numbered in order to ensure easy reconstruction. After

the strips are numbered, they are placed on a piece of Lexan 86.84 inches wide and 103.87 inches in length, cut into the shape of the hexagon. The scintillator, in groups of three, is then placed in the webbing, which had been scored and folded so it fits snugly with the scintillator triplets (see Figure 4). For light tightness and rigidity, each plane is wrapped in Lexan skins. A web layer of the skin material is routed between the scintillator triplets to provide flat gluing surfaces and a strong connection between the outer skins. The edges and ends of the planes have edge pieces made of flexible black foamed PVC to improve light-tightness. The orientation of the side rails and edge pieces is indicated in Figure 3. On the readout end of the plane, the PVC edge pieces are partially grooved to route the fibers to their exit points at the end of the assembly. The green fibers are extended past the end of the hexagonal plane and routed out of the detector where it transitions to a clear optical cable via optical connectors¹ [4]. When building this prototype plane we carefully measured the dimensions of the plane and drilled fixturing holes into the preparation table in order to ensure uniformity of each scintillator plane at William and Mary.

4.1 Gluing the Plane

We first remove the top layer of scintillator to a clean staging area, stage the parts while making sure the scintillators stay clean and lint free, and making sure to put each piece in the same orientation and in order; keeping each group of three together and off-set them from the next pair. After the scintillator has been cleaned, a layer of adhesive is spread over the bottom Lexan skin. We are using a 3M DP190 structural adhesive with a cure time of 90 minutes and a pneumatic gun to mix and dispense the structural adhesive. The adhesive is very viscous so must be carefully spread in order to not exceed the thicknesses tolerances of the plane. The PVC edge pieces and lower strips are laid into position on the carefully marked bottom Lexan skin. The

¹DDK optical connectors

adhesive is then applied to the gaps between the strips and the web layer is carefully positioned over the bottom scintillator strips. The vacuum table has been equipped with fixturing holes that fit into the PVC pieces surrounding the plane in order to give each plane the same dimensions. We have also had acrylic bars machined in a sawtooth pattern to equally space the bottom triplets in the scintillator planes. We then cover the assembly with a vacuum seal and cure it overnight. On the second day, we apply glue to the top of the webbing and lay the upper strips, then apply another layer of glue over the top scintillator and place the top Lexan skin over the plane. The assembly is again covered in a vacuum seal and cured overnight.

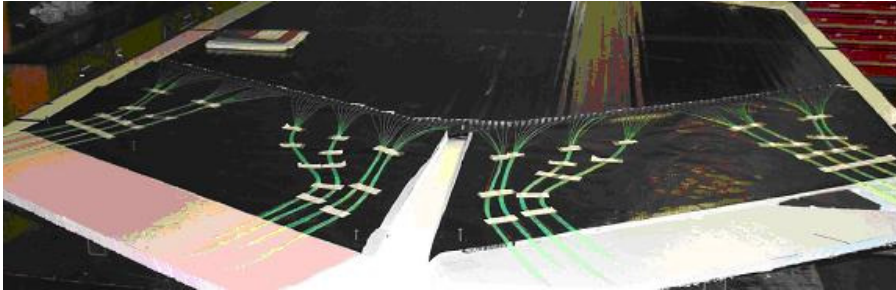


Figure 5: Diagram of the finished plane including fibers routed onto the Canvex sheets. The plane only needs to have the fibers placed in optical connectors and have a second piece of Canvex sheeting placed over the fibers in order to make them light tight.

4.2 Fiber Routing and Optical Adhesive

Once the plane has been constructed we apply RTV, room temperature vulcanization, silicone over the edge pieces located at the bottom of the plane, and route the mirrored fibers into each of the 127 extruded scintillator strips that make up the plane. One of the important finishing aspects of finalizing planes 1 and 2 was gluing the fibers with the optical epoxy in each of the 127 inner detector scintillator strips. During future construction there will be a gluing machine that will allow us to glue each of the fibers in the plane in a much more efficient but for planes 1 and 2 the fibers were

all glued by hand. This involved using syringes with a 45 degree angle needle so it would be able to route through the end combs of the plane.

There were many setbacks in the gluing process due to back pressure from the epoxy. As we tried to glue the longer strips the back pressure would leak through the RTV seal flooding the PVC combs with epoxy. This led to some partially glued scintillator strips within the plane. A temporary solution of putting the needle through a rubber stopper lubricated with vaseline and forcibly apply pressure to the hole in the scintillator.

The fibers are routed onto a piece of reinforced black polyethylene sheeting² to ensure light tightness and to protect the fibers during shipping and installation as well as whatever repairs will need to be performed later in the experiment. The fibers are routed in strict patterns that have been traced on the polyethylene sheeting to ensure that the fibers do not interfere with the other components that will be added to the planes at a later date. These strict patterns are also due to the 2.5" bend radius tolerances of the fibers. The fibers are then routed into the optical connectors³ which hold 8 fibers each, which will later be use to couple the WLS fibers to clear optical fibers. We transition to the clear optical fibers because they have less attenuation as the light travels to the PMTs then the green fibers.

The fibers and connectors are then polished with our fly cutting machine to maximize the light reflection between the WLS fibers and the clear optical fibers. The fly cutter, which has two rotating diamond tipped bits will make two passes on the optical connectors and fibers: a rough cut where the excess fiber lengths are cut, and a finer cut that involved not only cutting the fibers but also cutting off approximately 0.5 mm of the optical connectors to ensure a smooth finish. The clear optical fibers are then routed to PMTs which will convert the photoelectrons transferred through the fibers into a current and from there into the electronics which help analyze the

²Canvex

³DDK optical connectors

particles that are passing through the detector.

Before we receive the fibers they are mirrored with 99.999% chemically pure aluminum (approximately 250 nm thick) and cut in 7 different lengths. There are a set number of lengths so that we can minimize the amount of excess fibers. After the fibers are polished by the fly cutter the connector boxes are screwed to a thin length of aluminum to keep them in place, and another piece of Canvex is placed over the fibers and taped along the edges to make it light tight, thereby finishing the plane construction. A picture of a mostly finished plane with the fibers routed out into the optical connectors is shown in Figure 5. One of the main overall goals for this year was to create three new scintillator planes for the MINER ν A detector. One of the first projects that needed to be completed was to finish the first prototype plane constructed over the summer, and send it to the University of Rochester for structural testing.

This year we have developed procedures for the preparation and construction of the MINER ν A detector planes. These methods determined the most time and cost effective means of handling the full scale operations slated to begin later this year. In preparation for the production of the full module prototype and the transition to the mass production of planes over the course of the next year, the lab has undergone massive changes. A reorganization of the High Energy Group at William and Mary has transferred the MECO experiment to the third floor so the entire basement lab can now be dedicated to production. With this reorganization we now have the space for two full vacuum and preparation tables, as well as space for the inner and outer detector cutting tables. Each of the new vacuum tables is being outfitted with a base of 80:20 steel which provides stability as well as a level surface for the planes. In order to ensure a proper vacuum seal on the table the surface will be coated with a nonporous sheet of laminate.

5 Outer Detector Scintillator

Another of the goals of this project was optical testing and data analysis of the outer detector scintillator. We had cut eight towers worth of outer detector scintillator during this past summer, and our initial prototype planes only need 6 outer detector towers. We used the two extra outer detector towers to determine the effective light output of the outer detector in order to determine a cost effective solution to optically couple the WLS fibers to the outer detector scintillator.

The outer detector scintillator is arranged in a hexagonal array of 8 rectangular

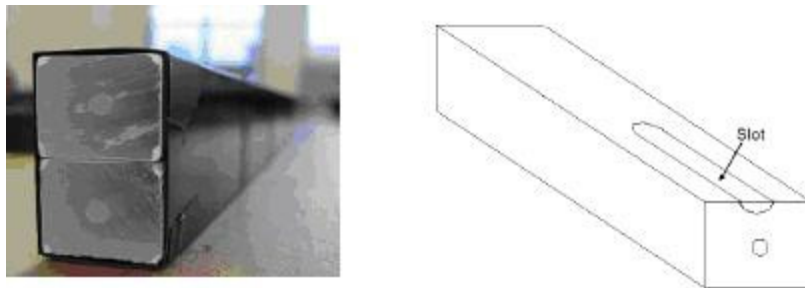


Figure 6: The figure on the left shows the Lexan wrapped outer detector scintillator pair. The figure on the right shows a diagram of the top OD strip with its slot in the top and the fiber role.

scintillator strips. The outer detector towers are arrayed in 4 rows of decreasing size with 2 scintillators nested on top of each other, and wrapped with Lexan for light tightness. The outer detector scintillator strips are rectangular in shape because they do not need the directional specificity that the inner detector scintillator needs in charting particle reactions. Since the OD scintillator strips are only used in hadron calorimetry, the light output of the outer detector scintillator does not need to be optimized for maximal reflection, but uniformity is important.

The fibers are then routed through a slit machined from the top scintillator (Figure 6). The slots are machined so that the fibers from both strips can be routed out through the top of the scintillators and out through the frame and into the photomultiplier tubes. A picture of one tower of OD scintillator, with its fibers routed out

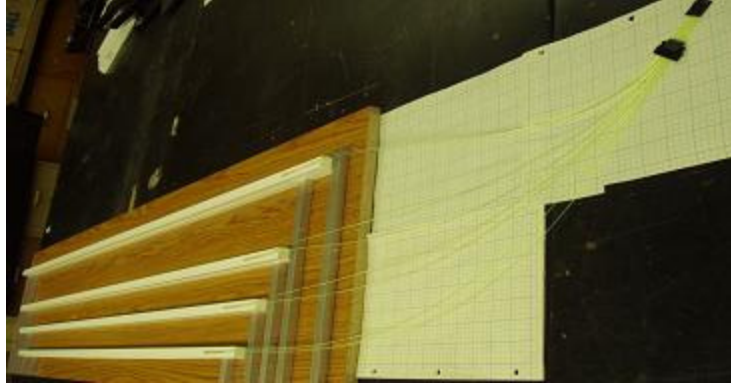


Figure 7: Fiber Routing of one OD scintillator tower. A set of 4 OD doublets is routed into a single connector.

into a connector is shown in Figure 7. Figure 7 also shows a fixture table made by Dan Damiani to ensure that each of the scintillator pairs are the right length and will fit in their steel slots.

In trying to decide the best and most cost effective way to route the fibers through the outer detector scintillator, we tried a number of combination of end treatments and epoxy quantities. We used an optically clear, low viscosity epoxy consisting of Epon 815C and Epi-Cure 3234 in order to secure the output of the fibers in the OD scintillator. The epoxy is necessary to provide better optical coupling between the WLS fiber and the scintillator.

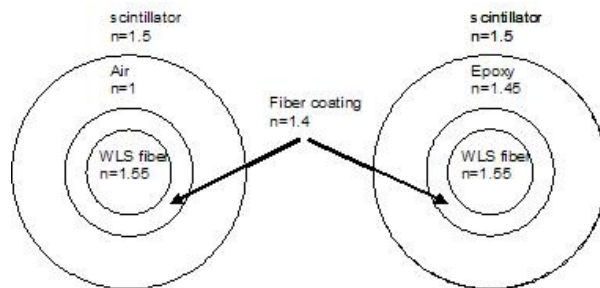


Figure 8: Diagram of WLS fibers inside the fiber holes of the ID or OD scintillator. On the left is a picture of a fiber without optical epoxy, while on the right is a picture of a WLS fiber optically coupled to the scintillator with epoxy

Figure 8 shows a diagram of the scintillator with and without the epoxy. In

the diagram on the right demonstrates the large changes in the indices of refraction indicate that the photons that are produced in the scintillator will not always be transferred to the fibers. However, the optical epoxy would significantly boost the energy deposition in the WLS fibers. As shown in the figure on the left, because the optical epoxy has a much closer index of refraction to the fiber and the scintillator the photons is much more likely to go through. Studies over which epoxy is the most cost effective as well as which epoxy produces the best result were performed last year by Meghan Snyder.

We used a Bicon white reflective paint in order to ensure light retention within the strips. The purpose of the Bicon paint is to improve the reflection into the scintillator from the 50 % of photons that travelled away from the readout end of the scintillator towers. In the table below is a list of the different combinations created:

Table 1: Combinations of end treatment trials on the OD scintillator doublets to determine best light yield of OD scintillator strips. The 0's represent when the end treatments was performed on the scintillator and the x 's are when it was not.

Sample	Slot Length (mm)	Scint. Length (mm)	End Painted	Top Painted	Fibers Glued
1	1708.4	1700.5	0	x	x
2	1547.0	1539.1	0	0	0
3	1451.8	1443.9	0	0	0
4	1356.4	1348.5	0	0	0
5	1708.4	1700.5	x	x	0
6	1547.0	1539.1	x	x	0
7	1451.8	1443.9	x	x	0
8	1356.4	1348.5	x	x	x

Each of the outer detector pairs was subjected to light yield testing at Hampton University. The schematic for the light yield testing of the outer detector scintillator pairs is shown in Figure 9. Two narrow scintillators were used to provide a trigger from cosmic ray muons and particles and were placed on either side of the OD scintillator. Each time one of these narrow scintillators read an event they would trigger the electronics to read a signal. The WLS fibers were then coupled to a 1-1/2" PMT and the charge was collected from each trigger event.[6]

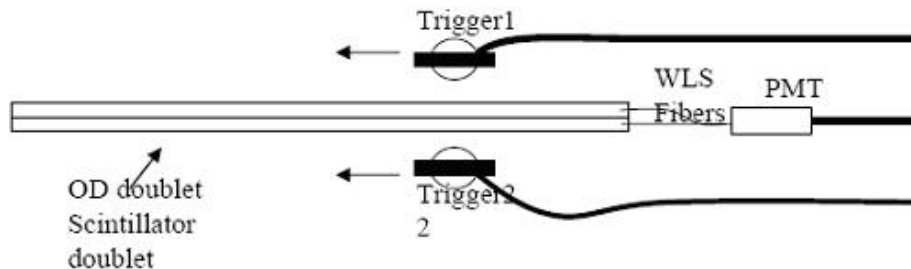


Figure 9: Diagram of the setup for testing the for OD pairs. The diagram shows the test setup for one of the OD doublets. The triggers are placed on top of the doublet, while the WLS fibers are routed through the doublet and also read into a PMT [6].

5.1 Results

The light yield data of the outer detector scintillator was analyzed with the program PAW. PAW, the Physics Analysis Workstation, is an interactive, scriptable computer software tool for data analysis and graphical presentation in high energy physics. It was developed by CERN to process large amounts of data and is based on the Fortran programming language.

Charge collection tests were measured at six different points on the scintillator pairs. The narrow scintillator triggers were moved down the length of each strip stopping at intervals of 2 cm 5 cm, 10 cm, 20 cm, 30 cm, 40 cm, 50 cm and 60 cm. Approximately 4000 events were triggered, which corresponds to approximately 1000 tracks intersecting the doublet. Our initial findings showed that we see attenuation above 20 cm, as well as roll off below 20 cm. This roll off is primarily due to the fact that the OD scintillator is slotted to allow for routing the WLS fibers out through the steel slots to the PMTs. After this we see a normal decaying curve as the light falls off from the readout end. There are a few “tails” to the end, which may be due to imperfect reflections at the ends of the OD pairs; the fibers have a reflecting mirrored end which will reflect the light that had propagated in that direction.

The data received from Hampton was analyzed with ROOT, a software package created by CERN. ROOT was used to create histograms as well as plots of the

output data from the OD scintillator strips. Several scripts, which appear in the appendices, were written with the help of Daniel Damiani to analyze the data and create the histograms and plots. Below is a graph of the initial data from by the charge collection tests.

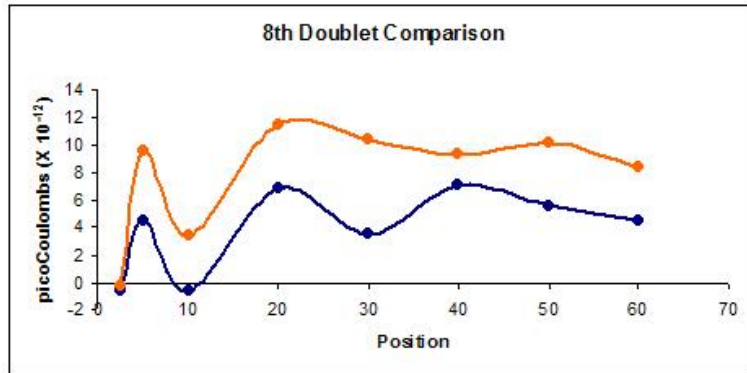


Figure 10: The different distributions between the gaussian and averaged mean. The blue line represents the gaussian mean, while the yellow line represents the calculated average. The data plot of the integrated charge measured in PicoCoulombs versus the length of the scintillator with length 1356.4 in Figure 10. It shows the differences between the calculated and averaged mean.

Charge was collected at each of the positions listed above, so each doublet will output 8 graphs for a total of 64 graphs. Each of these plots was fitted to a Gaussian distribution so we can find the mean of each of the peaks of the graphs. There were several challenges involved in this analysis, each graph had a pedestal due to the electronics used in the charge collection tests. Fluctuations within the peak of the pedestal resulted from the way the cosmic ray muon detection system was setup. Depending on the trajectory of the incoming particles, specifically in the case of the cosmic particles going through the narrow scintillator strips that serve as a trigger but does not go through the scintillator below, then the triggering scintillator will tell the electronics to detect an event, even though the particle did not go through the OD scintillator. This leads to a null result which accumulates at the pedestal. The complications arise from the fact that the pedestal did not have a fixed value and so

the boundaries of the Gaussian had to be able to change depending on the pedestal placement. There were also a few data sets from the PMT that had a different gain on the detectors which increased the data by a constant factor that needed to be taken care of in the script. Since the pedestal is often much higher than the data peaks, a zoomed image of each of the graphs was created and an example is shown in Figure 11.

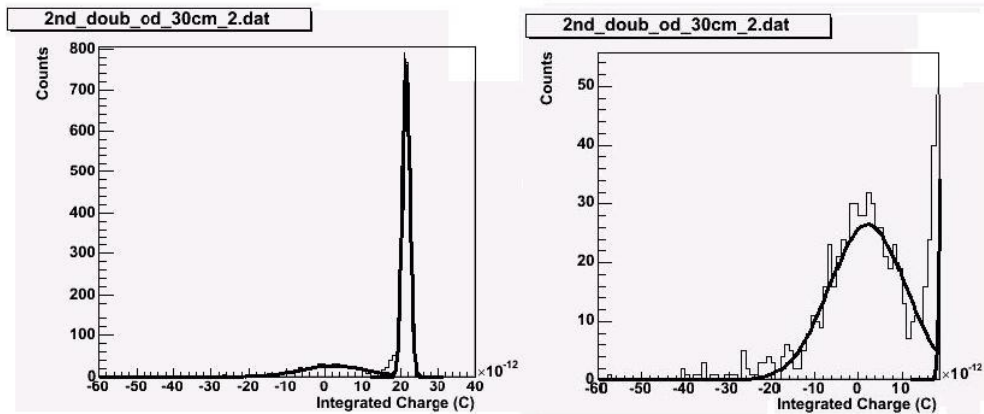


Figure 11: The plots represent the gaussian fits of the data peak and the pedestal taken at the 30 cm point on and OD doublet that has had its top and ends painted and its fiber glued into its slot. The graph on the right is a zoomed version of the graph on the left.

In order to perform a check on the gaussian fits of the data peaks we also did a calculated mean of each of the graphs above the pedestal. The necessity of this check can be seen in Figure 12. The tail of the gaussian is raised due to the fact that the pedestal is too close to the data peak, so it is interfering with the gaussian fitting curve.

The graphs shown in Figures 13 and 14 shows the results of the OD scintillator testing. The fits of each of the doublets was then placed on the same graph in order for us to analyze the differences in the end treatments of each of the scintillators.

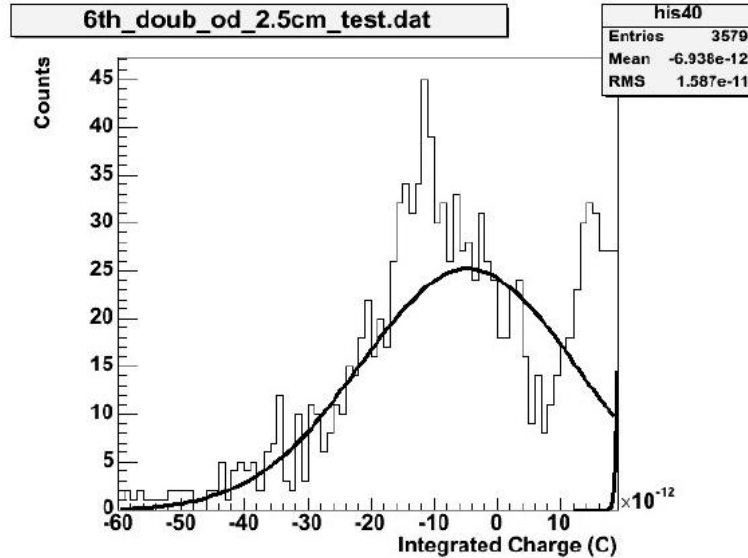


Figure 12: Pedestal leading edge interfering with gaussian fit of data. The data peak and the pedestal are very close together so the left edge of the pedestal is interfering with the fit of the data peak. (The pedestal can be seen rising on the right hand side of the plot).

Along the x -axis we have the positions that each of the scintillator was tested. Along the y -axis we have the charge detected in the scintillator. Each strip is represented by a different line. There are two points that are centered at zero; the data points for these positions were never taken. The error bars represent the possible error in measurement determined by the fitting curve of the signals. There were also suspicions that OD doublet 2, the red curve depicted in the results of the OD testing, had a broken fiber which would lead to anomalous data points. As expected, it was shown that the scintillator without paint or glue performed below those strips with either or both of the paint and glue. The strips that had glued in their slots, and therefore had greater optical coupling consistently performed better than those without. There were some anomalies in that the three strips that had both the optical epoxy and had the Bicorn paint on both ends, did not have the highest output. However, the graphs do indicate that the strips with the Bicorn paint (when compared to the strip without the paint) did show improved results. The graph also show that painting the top of slots has a significant affect in the light yield as it progresses away from the

read out end of the scintillator.

Due to these results subsequent OD towers will all have the fibers glued in the slots as well as painted with the Bicon paint along the top and ends before being wrapped in Lexan for light tightness. However, due to time and cost constraints we will not be putting the epoxy through the entire strip.

We will only be gluing the slotted end of the strip to improve uniformity; while this decision does save time and money, it led to some challenges as well. Since there is no barrier where we would like to glue to stop in my initial attempts in gluing only the slotted end of the OD strips the glue would seep into the fiber holes before it would harden. After several different procedures for gluing the slots we found a procedure that involves two gluing steps. One in which we place a small amount of epoxy in each of the fiber holes and allow it to harden. Then fill the remainder of the slots with epoxy. This procedure allows us to use a much smaller amount of glue, even though it takes about the same amount of time as filling the entire strip.

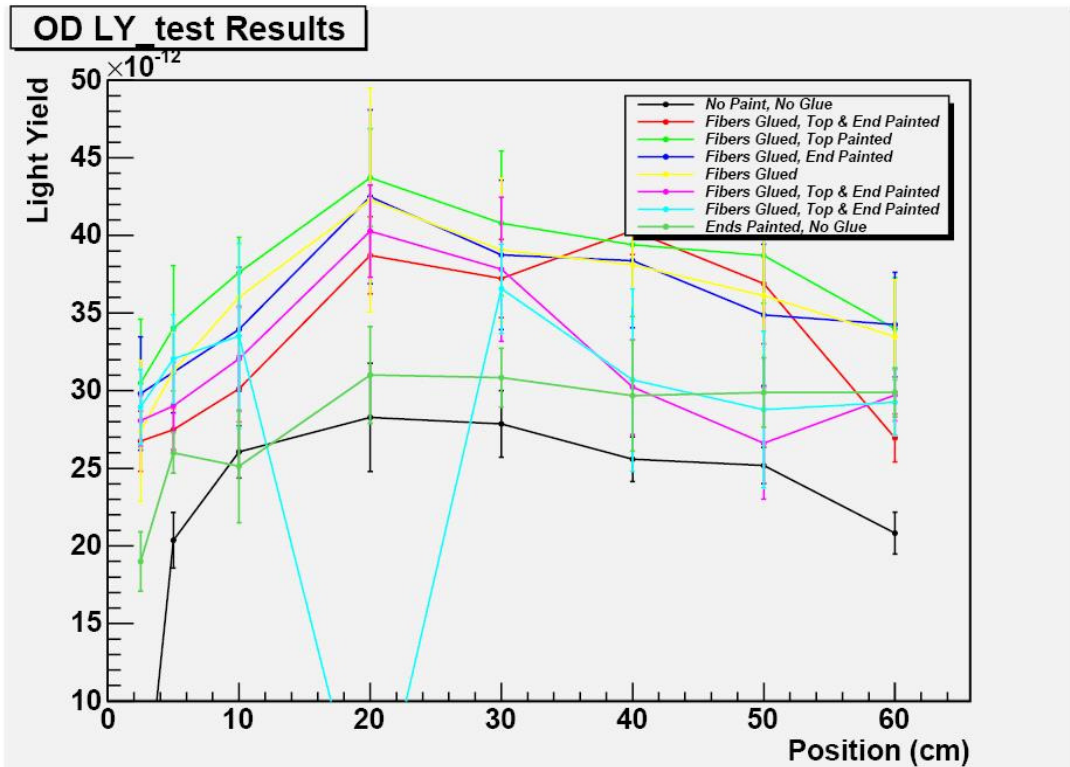


Figure 13: Results of outer detector strip testing with a calculated mean. Along the x -axis are the positions triggered on each of the OD doublets. Along the y -axis is the charge collected by the PMT measured in nanoCoulombs.

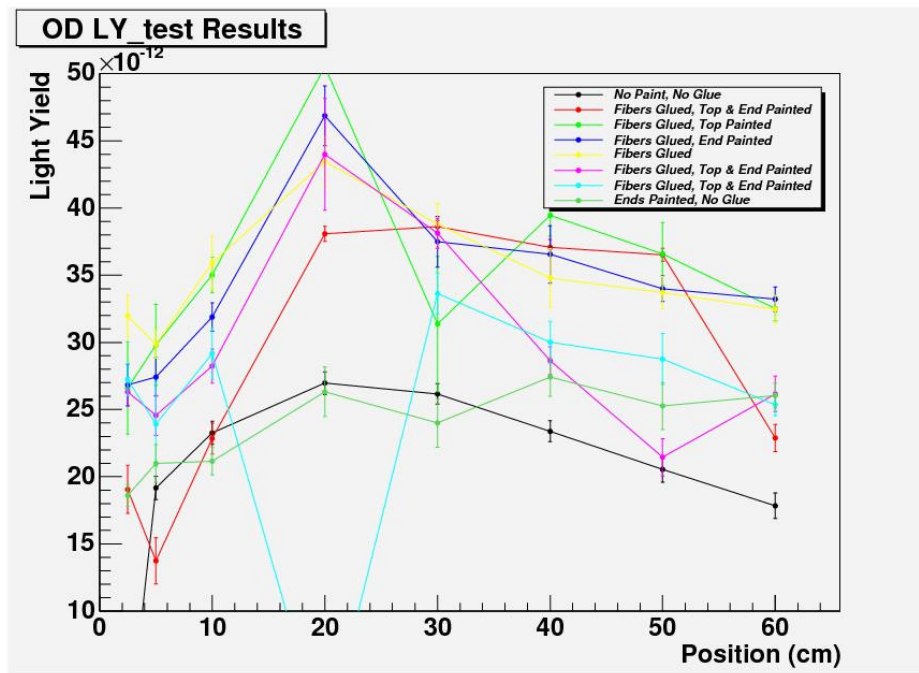


Figure 14: Results of outer detector strip testing with the gaussian average. Along the x -axis are the positions triggered on each of the OD doublets. Along the y -axis is the charge collected by the PMT measured in nanoCoulombs. This graph shows much more uniform curves than the plot of the gaussian mean of each of the data peaks.

6 Monte Carlo Simulation

Monte Carlo methods are a widely used class of computational algorithms for simulating the behavior of various physical and mathematical systems, and for other computations. They are distinguished from other simulation methods (such as molecular dynamics) by being stochastic or nondeterministic in some manner. In our current Monte Carlo simulation a random number generator allows the simulation to randomize events as opposed to deterministic algorithms. Because of the repetition of algorithms and the large number of calculations involved, Monte Carlo is a method suited to calculation using a computer. Our Monte Carlo simulation represents a radioactive source producing particles that will interact with the inner detector scintillator utilized in the MINER ν A project.

6.1 Radioactive Decay

All nuclei heavier than lead have a finite probability of decaying spontaneously into another nucleus plus one or more lighter particles. One of the decay products may be an alpha-particle, or a nucleus with more neutrons than it can stably maintain may decay by emission of an electron from the nucleus, which is also known as beta-decay and will convert a neutron into a proton. After alpha or beta decay, the residual nucleus may be left in an excited state. In this case, a transition to a state of lower energy of the same nucleus will occur almost immediately with the emission of a gamma ray. In our Monte Carlo simulation we are working with a ^{137}Cs source, which produces an electron as well as the daughter nucleus, ^{137}Ba . This nucleus has a very short half life of approximately 2.6 minutes and then decays into a gamma, with energy 0.662 MeV, and the stable isotope ^{137}Ba .

6.2 Energy Loss and Range of Beta Particles

Because of its ionizing action, as shown in Figure 15, a charged, incident particle in matter will continuously lose kinetic energy, and the particle will subsequently come to rest after traversing a path length called its range. For a particle of known charge and mass, there will be a unique average range associated with each incident energy.

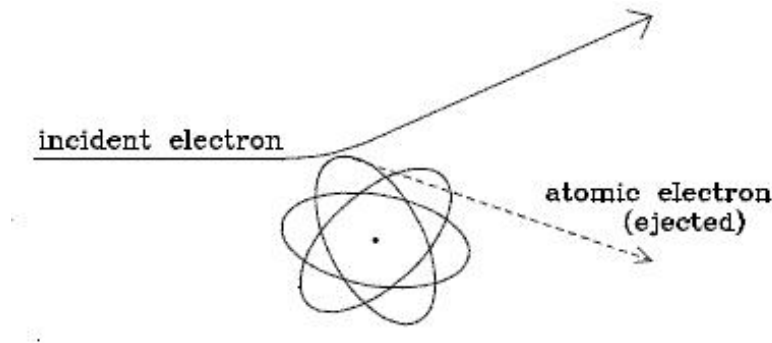


Figure 15: Ionizing Action of Incident Electron [12]

A formula can be theoretically deduced for the rate of energy loss and through this the range of a particle of known mass, charge, and initial velocity. In a particular material of known electron density and ionization potential, which in our case consists of the different types of materials used in our Monte Carlo Simulation including: zinc, iron, air, scintillator, and the WLS fibers. In each interaction with atomic electrons, however, an incident electron may be scattered through small or relatively large angles, and as it traverses the material it may follow a rather winding path, especially at low energies. Therefore, the actual path of the electron may be considerably longer than the observed distance that it penetrates into the material.

6.3 Absorption of Gamma Rays

Gamma rays, or high-energy photons, can interact with matter by three distinct processes. The first of these three interactions is Compton Scattering. Compton Scattering refers to a photon-electron collision in which the energy lost by the scattered photon is given to the recoil electron. The second of these interactions is defined by the photoelectric effect where the photon is absorbed by the atom as a whole, and releases an electron with kinetic energy equal to $E_\gamma - E_b$, where E_γ is the photon energy and E_b is the relatively small binding energy of the electron in the shell from which it is released. The final interaction type that gamma rays can have is pair production. Pair production happens if the photon has energy greater than 1.02 MeV, it can create an electron-positron pair in the neighborhood of a nucleus. The probability of each of the three processes taking place in a given thickness of material depends on the energy of the photon and the atomic structure of the material. The total probability for interaction of photons in a material is the sum of the probabilities of the three processes and varies with photon energy.

6.4 Compton scattering

The main interaction taking place inside the scintillator is Compton scattering. A diagram of the interactions involved in Compton scattering is shown in Figure 15. The process of Compton scattering can be described as a relativistic collision, in which a photon of a specified energy Q_0 collides with an electron. The struck electron is treated as a free and stationary particle, which is a reasonable approximation for a target composed of low- Z material, in which the binding energy of the struck electron is small in comparison to the shift in energy of the scattered photon. After the collision the photon has an energy Q and a direction θ , while the electron, whose only energy before was its rest mass, now has an energy, momentum \mathbf{p} , and angle ϕ (where ϕ is measured from the initial photon trajectory) respectively. Using

conservation of energy and momentum we can write the relation between the photon and electron as follows:

$$Q_0 + m_0c^2 = E + Q \quad (6)$$

$$\mathbf{p}Q_0/c = \mathbf{p}'Q/c + \mathbf{P} \quad (7)$$

If we square both sides of each of those equations and rearrange them so that the unknown values of the electron energy and momentum are on the left side you get the following equations:

$$(Q_0 - Q)^2 + 2(Q_0 - Q)m_0c^2 + (m_0c^2)^2 = E^2 \quad (8)$$

$$Q_0^2 - 2Q_0Q\cos\theta + Q^2 = c^2p^2 \quad (9)$$

Then combining these equations we get an equation that is only dependent on the photon values

$$2Q_0Q(1 - \cos\theta) - 2(Q_0 - Q)m_0c^2 = 0 \quad (10)$$

After that is complete the photon energy is placed on the right hand side of the equation and the angle dependence is placed on the left hand side of the equation. And since the photon energy is quantized we can substitute

$$Q = \frac{hc}{\lambda}$$

in for Q and Q_0 :

$$\frac{\lambda}{hc} - \frac{\lambda_0}{hc} = \frac{h}{m_0c} (1 - \cos\theta) \quad (11)$$

From this equation we can determine the Compton effect in terms of wavelength

with the following equation:

$$\lambda - \lambda_0 = \frac{h}{m_0c}(1 - \cos\theta) \quad (12)$$

From here we can determine from the photon energy and geometry of our detector what the expected energy deposition from the scintillators should be [8].

7 Mapsim

The Monte Carlo we were using in order to simulate the electron deposition into the MINER ν A scintillator with a radioactive source is called Mapsim and was initially designed by two physicists involved in the MINER ν A project, Leonidas Aliaga and Alberto Gago from Pontificia Universidad Catolica del Peru. It was designed for source testing at Fermilab. Mapsim is run on a simulation software package designed to describe the passage of elementary particles through matter called GEANT4. The name GEANT is from the acronym “GEometry ANd Tracking”. GEANT was first developed at CERN for high energy physics experiments. GEANT works in conjunction with a library system called CLHEP. CLHEP, which was also created by CERN, is short for a Class Library for High Energy Physics and is a C++ library that provides utility classes for general numerical programming, vector arithmetic, geometry, pseudorandom number generation, and linear algebra, specifically targeted for high energy physics simulation and analysis software. Mapsim has many source files that determine the detector geometry, the type, time, and energy of the particles that are produced in the decay, as well as different particles that could be introduced into the simulation to determine the scintillators responses to different particles.

All of these files including the files that right out the histograms are hard coded into the program, so that in order to change any of the parameters located in these files the Mapsim program had to be recompiled. This proved especially challenging

because every time we had to change the detector geometry the entire program had to be recompiled to create another executable.

The Mapsim program also had a visualization macro that allowed certain parameters of the simulation to be changed without recompiling the program. These parameters dealt mainly with the creation of the viewer, and the viewer orientation. The macro also controlled the visualization of the event tracking and would allow us to change the parameters of the source, i.e. energy, trajectory, as well as the type of particles emitted.

7.1 Geometry

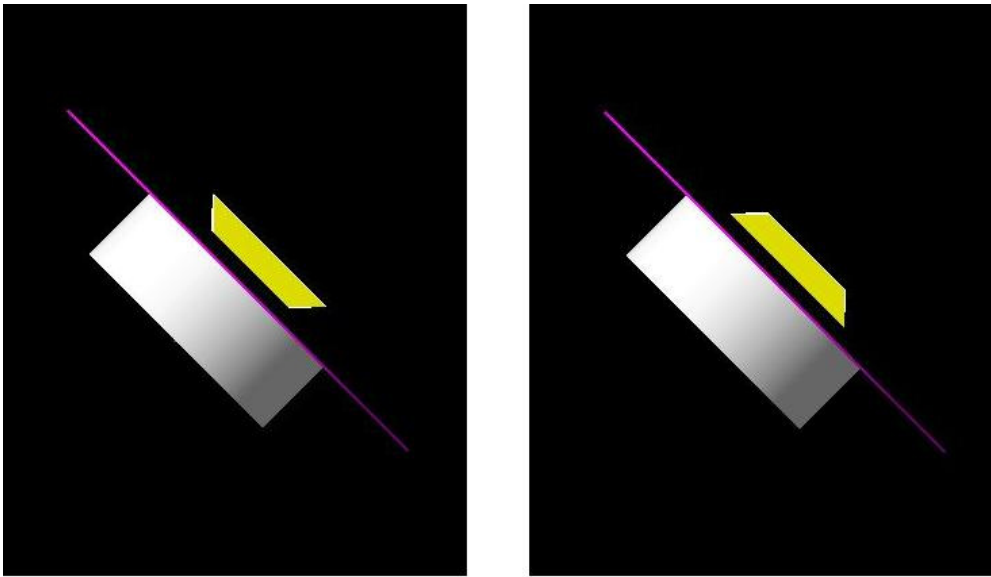


Figure 16: Volume Geometry of the MapSim Monte Carlo Simulation. The graph on the right represents the initial configuration, while the graph on the left represents a 180° flip of the plane in the x direction.

The geometry of our detector simulation is shown in Figure 16. Surrounding the ^{137}Cs source is a zinc cylinder with a radius of 7.3 cm. Within the zinc cylinder there is an air cylinder 1 cm in diameter to allow the source to emit beta particles and gamma rays without the dense metal to shield the scintillator. Below the cylinder there is an plate of iron of 1 mm thickness which absorbs the beta particles emitted

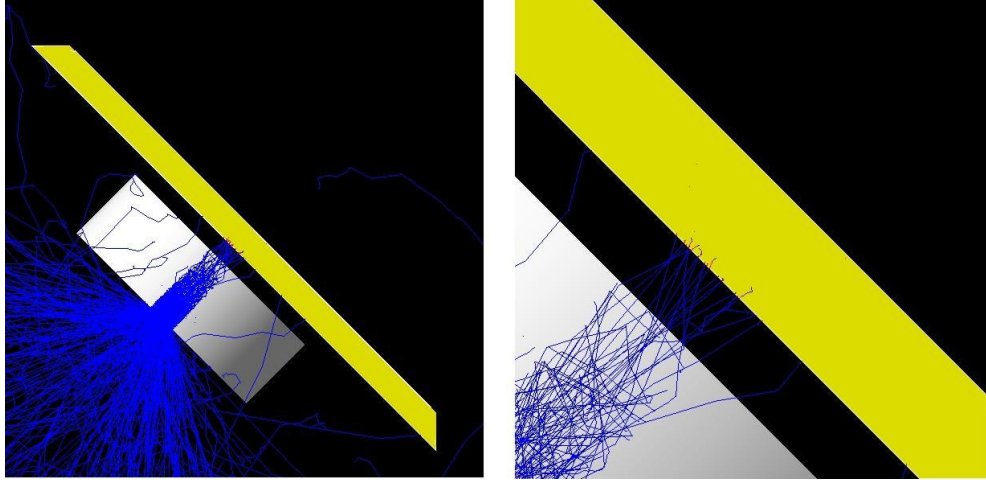


Figure 17: The figure on the right shows the zinc encased source without the thin layer of iron to absorb the electrons produced by the decay of the ^{137}Cs . The figure on the left is a zoomed version of the right hand side picture showing slight penetration of the electrons into the scintillator.

from the radioactive source but allows the photons through. This plate was later put in place because we were seeing electrons penetrating into the scintillator a very small amount, causing an increase in the energy deposited into the scintillator. You can see in Figure 17 that the electrons are penetrating into the scintillator. The yellow shape below the plate of iron represent the strips of scintillator. The number of strips throughout the experiment changed as well as the orientation of the strips but the scintillator strips were always ID strips 91 cm in length.

7.2 Data

We varied the number of strips to determine the distribution of the energy deposition of the electrons in the scintillator. The maximum number of strips we used was 21, because as can be seen in Figure 21, the number of electrons created in the outermost strips was extremely small and heading toward a negligible amount of energy. Figure 16 shows another change that was made in the detector geometry. The strips were rotated 180° around the x -axis. This allowed the odd number strips to be facing the radioactive source while the even numbered shift faced away, as well as allowing more

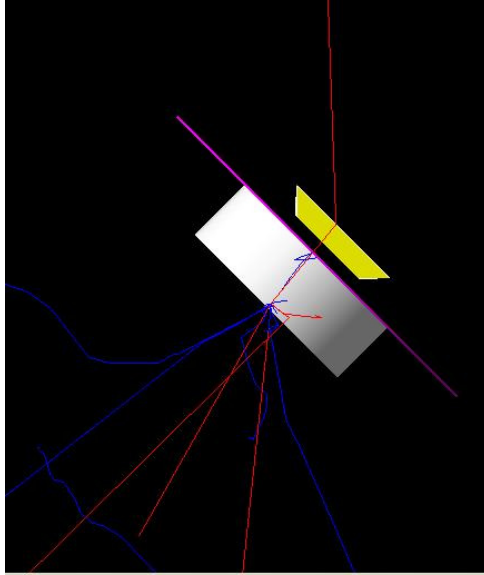


Figure 18: 1 event in the *Mapsिम* Monte Carlo simulation.

scintillating surface area to face the source.

Figure 18 shows one event in the *Mapsिम* simulation. In the graph, the blue tracks represent the electron trajectories, while the red tracks represent the gamma emission produced in the decay of the daughter particle ^{137}Ba . In the simulation, the stopping power of the sheet of iron can also be seen as the electron is blocked from entering the scintillator. There is some reflection of photons off the edge of the scintillator.

The anti-electron neutrinos that are created in the beta decay have been turned off due to their tendency to dominate the simulation and obscure the relevant data (Figure 19). As can be seen from the figure, the tracks from the electrons and photons, as well as the geometry of the detector are completely obscured by the neutrino tracks. In later runs we began to filter out the gamma rays as well, so the only tracks visible would be the electrons' tracks. The purpose of this was to see the electrons created by the Compton scattering of the photons in the scintillator very clearly without the gamma tracks to obscure our view of the scintillator.

The graph shown in Figure 20 shows the energies of the electrons being produced

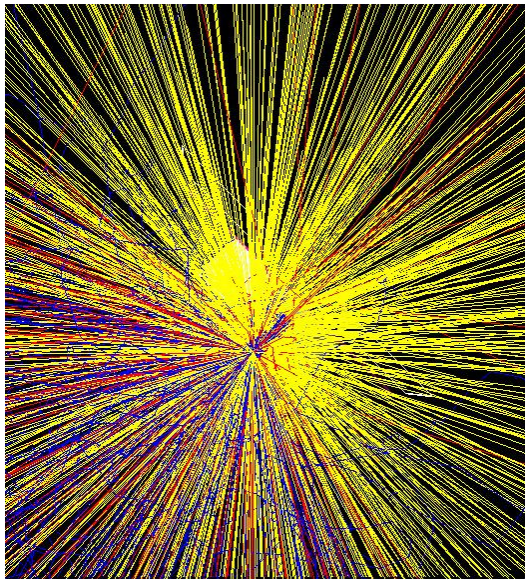


Figure 19: Neutrino dominated simulation. This figure shows an unfiltered visualization of 100 events.

by the decay of the ^{137}Cs . We can calculate the expected energy of the electrons from the Compton scattering and we find it to be approximately 0.372 MeV. The curve of the graph shows that the energy of the electrons produced falls off much more quickly than this. This could be due to multiple scatterings of the gamma ray emissions. After the gammas scatter, they have a smaller energy to impart to the recoil electron thereby bringing down the mean energy of the electrons.

7.3 Results

We began running the Monte Carlo simulations to test the idea of using sources for testing the uniformity of the scintillator inner detector planes. The number of PE per MIP that would be able to be detected by our PMT was extrapolated by a vertical slice test of the MINER ν A ID scintillator, and was discovered to be 212.7 keV per PE [4]. The average energy deposition of the photons Compton scattering in the scintillator varied as a function of the position of the scintillator relative to the source, as well as the orientation of the strips. However, when the scintillator was

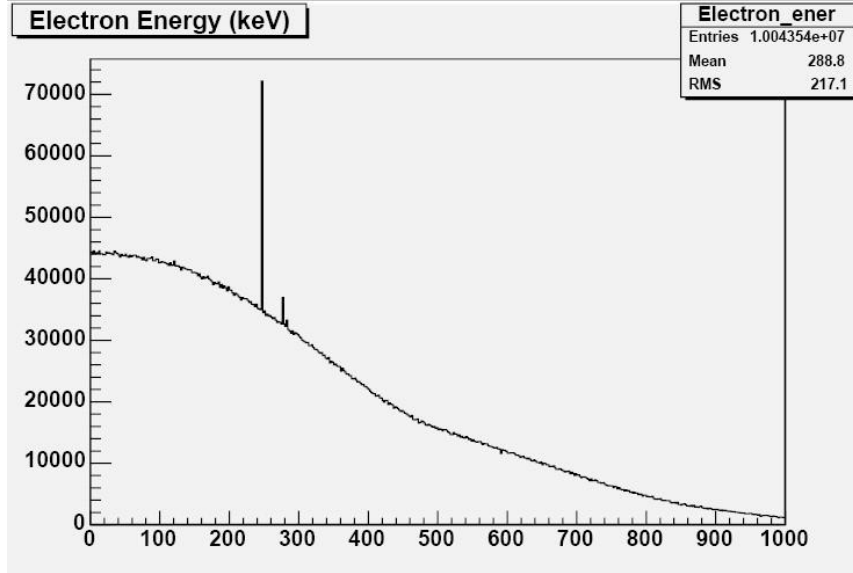


Figure 20: Energy deposition of the electrons produced in the decay of ^{137}Cs

directly underneath the source, the average energy deposition was 106.7 keV for 10^6 events. This meant that the average energy of the scintillator was well below a level that could produce even one photoelectron. Using Poisson statistics I determined that the probability of detecting even 1 photoelectron was 0.0148, with the probability of detecting more events decreasing by 2 orders of magnitude per photoelectron.

Table 2: Table describing energy deposition versus position and expected current for ^{137}Cs . The current calculations are based on a ^{137}Cs source of 10 mCi.

Orientation	Position (mm)	Num. of Events	Mean (keV)	Current (pA)
0	0	92	65.85	1.308
	8	990	69.29	1.113
	17	738	67.09	0.658
	33	362	68.16	0.367
180	0	96	67.11	1.237
	8	79	70.55	0.9116
	17	50	63.78	0.508
	33	28	119.2	0.271

By calculating the probability of detecting 1 photoelectron we were able to calculate an average current expected in a PMT with a gain of 10^6 . Using the Poisson statistics and the mean energy of the electrons deposited into the scintillator strips we were able to calculate an expected current for each of the positions.

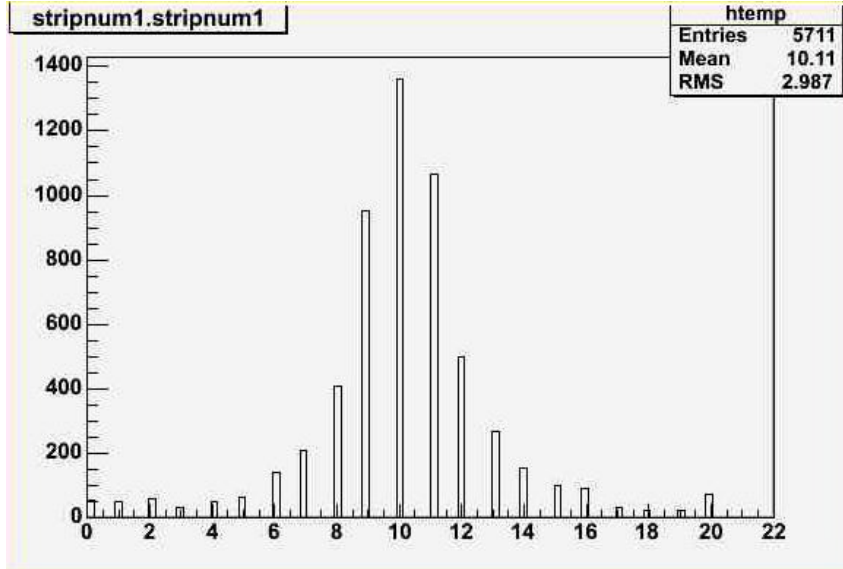


Figure 21: Distribution of 10^6 events over 21 scintillators strips. Strip 10 is a 0° oriented strip directly over the source

Figure 22 shows a plot of current versus position for both orientations of the single scintillator strip. The graph shows that the strip, when oriented at 0° has a much smaller PE current and energy deposition than when oriented at 180° . The 0° orientation refers to the scintillator strip oriented with its point facing the source. The 180° orientation refers to the scintillator strip oriented with its base pointing the source. 0° orientation and 180° orientation can also be referred to as top and bottom respectively. This is due to the much greater surface area exposed to the outer edge of the scintillator block. As can be seen in Figure 16 the leading edge in the 180° orientation has the entire base of the scintillator, while the 0° has a single point along the leading edge. This would mean that the gammas would have to travel farther into the scintillator without Compton scattering in order for it to deposit electrons in the scintillator strip. The 180° orientation should taper off as the source was moved farther away from the scintillator.

We have very recently discovered an error in the random number generator in the *Mapsim* simulation when trying to run 1 million events. The expected fall off

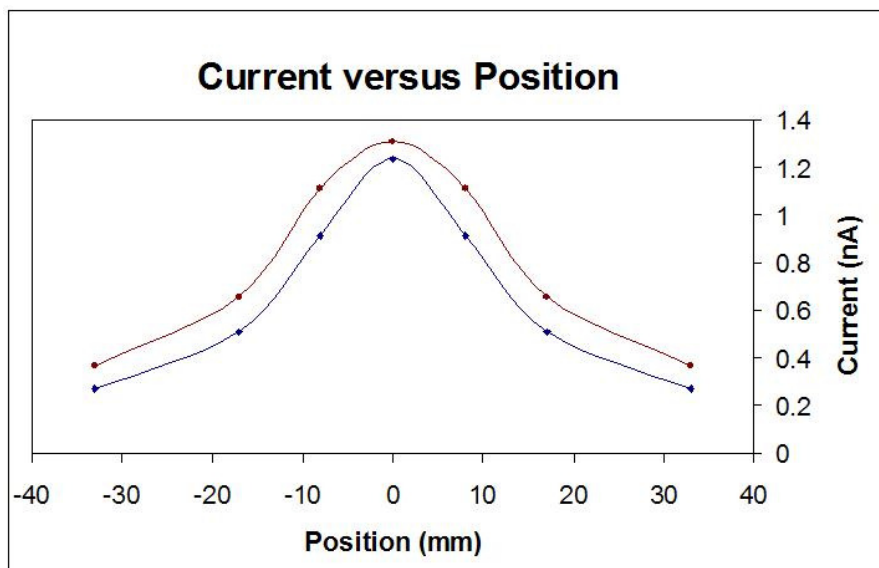


Figure 22: Depiction of a plot of the current measured in nanoAmps predicted by the Monte Carlo simulation as a function of the scintillators position with respect to the ^{137}Cs source. The red curve represents the current expected from a bottom scintillator strip, while the blue curve represents the current expected in a top scintillator strip.

of current as the scintillator moved away from the source did not occur. We are currently running ^{137}Cs source tests with a smaller number of events to correct this error. Recent plots of the data show a much more even distribution of current in the top and bottom strips. This even distribution is expected for a gamma source, since the particles are not very interacting and can penetrate farther into the scintillator than, for example, an electron.

Brian Wolthuis worked with the source placing it at different points along the plane and reading out the WLS fibers with a PMT. These uniformity measurements will tell us how well the scintillator will detect particles when fully constructed, including the multiple layers of Lexan and glue.

However the source testing had not yet been performed, because it was discovered that the ^{137}Cs source that was going to be used was only 3 mCi, which would drop the expected current almost by an order of magnitude, which means the signal would be indistinguishable from the background noise. This meant that either a stronger

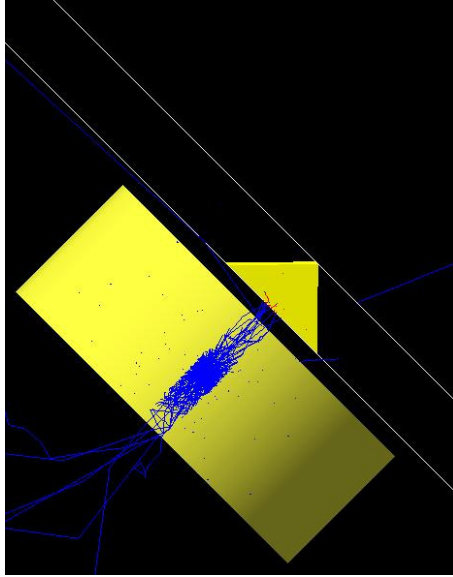


Figure 23: Example geometry for the ^{90}Sr source, which also shows 10^3 radioactive decays.

^{137}Cs source would need to be found or a different source will need to be used. There is a 10mCi source that could be used, however its collimator may not be compatible with our setup in terms of weight, the source has 80 lbs of lead shielding, and maneuverability.

Instead Brian started working with a ^{90}Sr source, with a strength of $4.16 \mu\text{Ci}$. The source was originally $10 \mu\text{Ci}$ in June of 1971, but ^{90}Sr has a half-life of 28.5 years so has decayed to less than half of its original value. Even though it is a much weaker source it produces higher energy beta particles. ^{90}Sr decays much like ^{137}Cs in that it emits a beta and a daughter particle that rapidly decays. The initial decay results in a lower energy beta of 546 keV and a daughter particle ^{90}Y . The ^{90}Y daughter has a half life of 2.67 days. The difference between the two radioactive decays is that while in ^{137}Cs the daughter particle emits a gamma of 0.663 MeV, the ^{90}Sr daughter particle decay results in a high energy electron of 2.28 MeV. A graph of the energy of the electrons coming out of the ^{90}Sr source is shown in Figure 24. The different energies electrons produced in the source show two distinct curves within the distribution.

The simulation geometry was changed to account for the new source and collima-

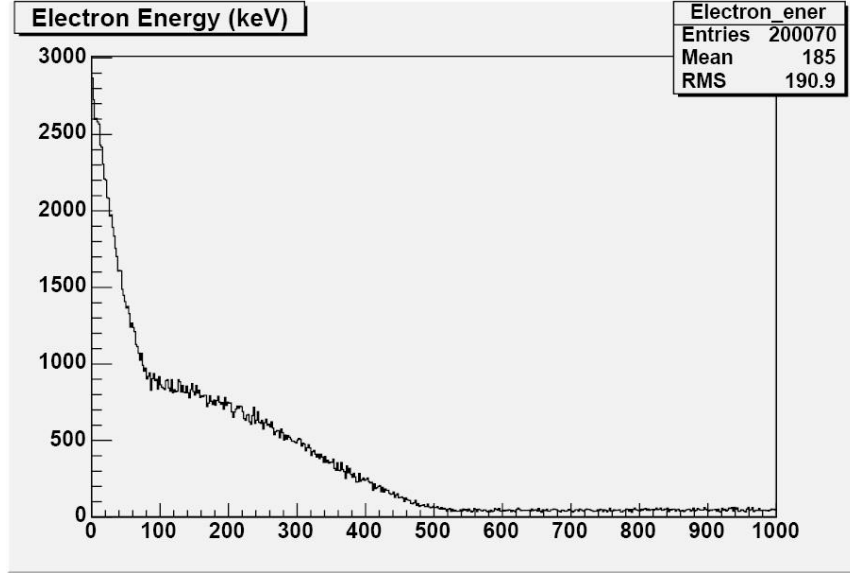


Figure 24: Energy distribution of electrons produced in the decay of ^{90}Sr . The graph represents the energy of every beta particle produced in 10^5 events.

tor. The plate of iron also had to be removed, because we were now detecting the beta particles directly instead of relying on the gammas Compton scattering within the scintillator. A diagram of the new detector geometry is shown in Figure 23. The collimator is much smaller with a diameter of about 5 cm. The air cylinder is only 8mm in diameter so it collimates the electrons created in the decay much better than the ^{137}Cs source. The collimator was also changed from zinc to brass (a combination of zinc and copper), which has a higher Z than only zinc.

Table 3: Table describing energy deposition versus position and expected current for ^{90}Sr

Orientation	Position (mm)	Num. of Events	Mean (keV)	Current (pA)
0	0	431	532.8	0.218
	4	291	556.6	0.138
	8	103	544.7	0.025
	12	10	444.9	0.003
180	0	3211	354.5	2.501
	4	3079	339.6	2.464
	8	3116	351.5	2.441
	12	2934	315.5	2.442
	17	1593	230.5	1.444
	22	274	164.4	0.242
	33	15	68.39	0.009

The drop off as the scintillator strip moves away from the center position shows that the collimator on the new ^{90}Sr source works much better than the collimator used with the ^{137}Cs source.

The graph of the data in the Table 3 is shown in Figure 26. The 0° orientation

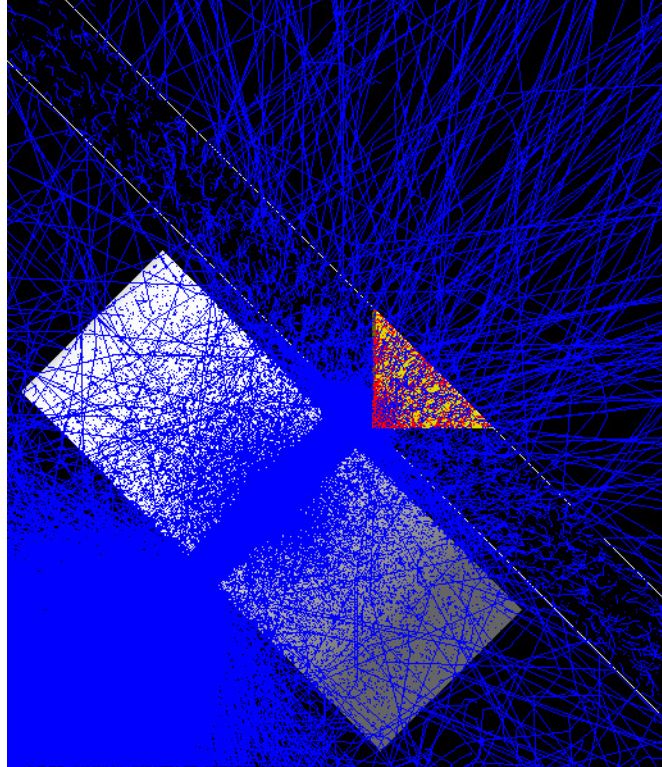


Figure 25: Geometry for the simulation of Sr90, this figure also shows 10^3 radioactive decay events.

has a much smaller current than the 180° orientation. The rest of the positions in the 0° orientation were not simulated because they did not receive any events. The 180° orientation shows a fall off as the position moves beyond the half width of the strip. Figure 25 shows a simulation of 10000 events. Figure 26 shows the plot of current versus position of the ^{90}Sr source. Unlike, the ^{137}Cs source the graph shows that energy deposition pattern is very well collimated. As the source moves away from the scintillator the current falls off dramatically for both the top and bottom strips. The beta particles produced in the decay of ^{90}Sr have far less penetration into the scintillator than the gammas produced in the decay of ^{137}Cs .

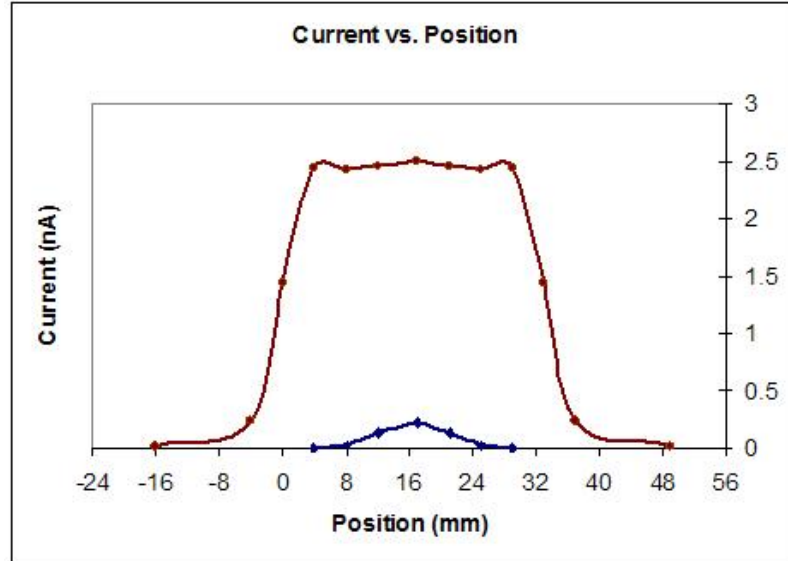


Figure 26: Depiction of a plot of the current measured in nA predicted by the Monte Carlo simulation as a function of the scintillators position with respect to the ^{90}Sr source. The red curve represents the current expected from a bottom scintillator strip, while the blue curve represents the current expected in a top scintillator strip.

To increase the signal to noise ratio Brian found the number of counts above a 1.5 PE energy threshold. We were able to simulate this in the *Mapsim* simulation. We plotted energy deposition in a histogram, in which we could manipulate the bin number and effectively count how many counts were above and below the threshold. We tested in our histograms a 1.5 PE threshold with a 1 PE threshold for reference. 1 PE is 212 keV, so any of the counts below 200 keV were discarded in our 1 PE threshold. The 1.5 PE threshold we set at 300 keV. We were able to determine the percentage of the events that produced more than one photoelectron by subtracting the number of counts below 1.5 and 1 PE from the total. We did this with both the 0° and 180° orientations. From here we could determine a ratio of the top and bottom strips to see the differences in energy deposition between the two strips. A table of the energy distribution from the *Mapsim* simulation of the counts is shown below. For the 1 PE cut off we saw a ratio of 5.75 between the top and bottom strips. For the 1.5 PE cut, there was a ratio of 4.5 PE between the 0° and 180° orientations.

In our simulation at the 1.5 PE cutoff we got approximately the same values in the difference in counts for the top and bottom strips as Brian has measured in his source testing of Plane 0.

Table 4: Table describing energy deposition versus the number of counts for ^{90}Sr .

Energy Range (keV)	Counts in 0°	Decrease in Counts in 0°	Counts in 180°	Decrease in Counts in 180°
0-50	10	396	125	1975
50-100	18	378	200	1775
100-150	29	349	250	1525
150-200	26	323	175	1350
200-250	34	289	165	1185
250-300	26	263	150	1035

The first column shows the ranges of energies that we segmented in the histogram into in order to determine the number of counts for a given energy. The second column represents the number of counts the simulation detected within the energy range of the first column. The third column shows the decrease of this energy from the total number of counts detected for the 0° orientation of the strips. The fourth and fifth columns are the same as the second and third for the 180° orientation of the strips.

Another source simulated for future source testings was ^{106}Ru . ^{106}Ru shares many characteristics with ^{90}Sr ; its initial decay results in a lower energy beta of 39 keV and a daughter particle ^{106}Rh . The ^{106}Rh has a half life of 35.36 hours. The decay of the daughter particle results in a much higher energy beta of 3.541 MeV. The energy of the second beta is bigger than the ^{90}Sr secondary beta by over 1 MeV. A graph of the energy distribution of electrons from the ^{106}Ru source is shown in Figure 27. This graph shows even more distinctly the differences in electron energies produced in the decay of ^{106}Ru . Since there is a greater difference in the initial and secondary betas produced in ^{106}Ru than ^{90}Sr , the graph produces a much more delineated structure. Since the lower energy electrons are produced in the initial decay of ^{106}Ru , and because they have a 100 percent probability of occurring as opposed to the secondary beta

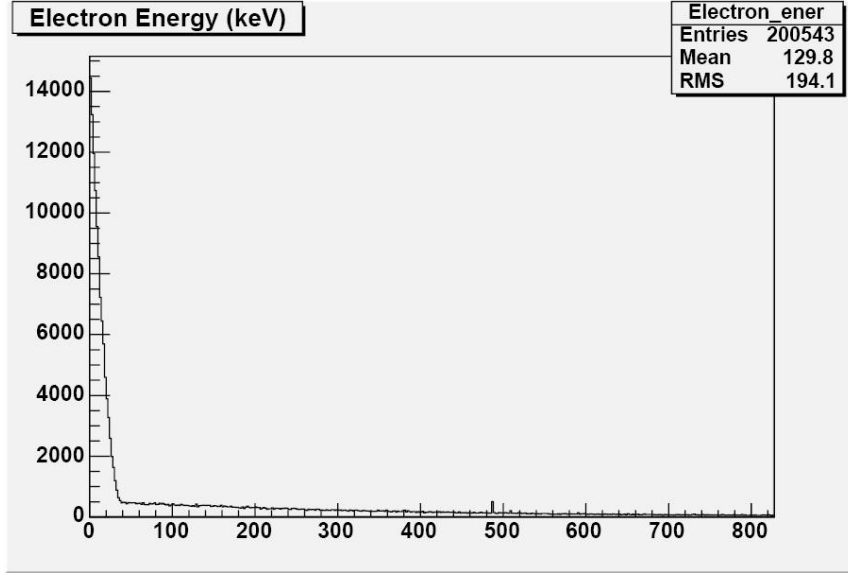


Figure 27: Energy distribution of electrons produced in the decay of ^{106}Ru . The graph represents the energy of every beta particle produced in 10^5 events.

which only has an 80 percent chance of occurring, there are many more lower energy electrons, which greatly reduces the mean energy of the electrons produced in the source. However, by counting above the 1.5 PE threshold we are able to obtain useful signals.

Both the current calculations and count distributions were done for the ^{106}Ru source at its 0° and 180° oriented center strips in order to compare these results to the ^{90}Sr source. The current calculated for the top strip was 0.19 nA, while the current for the bottom strip is 1.38 nA.

Table 5: Table describing energy deposition versus the number of counts for ^{106}Ru .

Energy Range (keV)	Counts in 0°	Decrease in Counts in 0°	Counts in 180°	Decrease in Counts in 180°
0-50	18	413	240	2970
50-100	35	378	450	2520
100-150	46	342	460	2080
150-200	41	301	350	1730
200-250	31	270	340	1390
250-300	21	249	270	1120

Table 5 shows the same data as ^{90}Sr in Table 4, but for ^{106}Ru . The ^{106}Ru has a more even distribution of energy deposition in the top and bottom scintillators

because the electrons have a higher energy they can penetrate more deeply into the scintillator. Although ^{90}Sr and ^{106}Ru have a similar count rate and mean energy, the rate of energy drop off in the counts favor ^{106}Ru as the source needed for experimental data. One of the greatest drawbacks with a ^{106}Ru source is its short half life. ^{90}Sr has a half life of 28.5 years while ^{106}Ru has a half life of only 1 year. The concern arises from the fact that we would need the source for testing over the next two and a half years. Therefore the end activity to be the same we would need a ^{106}Ru source would have to be 12 times stronger, while a ^{90}Sr source would experience only a 10 percent change in decay rate.

8 Conclusions

8.1 Construction

Planes 1 and 2 have been successfully sent to Fermilab so the first of the MINER ν A detector assemblies can be installed. A model of the scintillator planes has been produced to test for uniformity within the inner detector scintillator. We finished plane 1 and our third prototype plane. The new glue machine, which arrived at the time of writing this paper, because of its larger capacity and pressure will correct our back flow problems with the optical epoxy, and will also considerably decrease production time. Over the course of this year we have increased the uniformity of the planes and developed preparation methods for most of the construction of the inner detector planes. We have also run tests on both the inner and outer detector scintillators for uniformity and light output characteristics. Because of the increased light output, and greater uniformity in the scintillator strips, when they have been glued and painted, we have decided to both glue the fibers into the strips as well as paint both the top and ends with Bicron paint. These end treatments will be used on each of the subsequent OD towers along with the Lexan wrapping and black electrical

tape wrapping for light tightness.

8.2 Monte Carlo Simulation

The Monte Carlo simulations predicting the light read out of several strips of the ID scintillator were meant to coincide with experiments performed using radioactive source testing on plane 0. We were trying to determine the readout values from the actual plane. Although there were slight differences in the setup we hoped we could make an accurate comparison. We have discovered that for the PMT setup that we have currently, as well as the sizes of the sources that are available to us, we would be unable to detect a current from the 0° scintillator, which has a maximum current below 1 nA for a ^{137}Cs . However there should be enough counts for us to take uniformity measurements of the ID scintillator.

We changed the source to ^{90}Sr , which though smaller in radioactivity produces high energy beta particles, which are much more reactive than the gammas. This means that the betas will produce more current for the same amount of radioactivity as the gammas, as well as the fact that not as many decays need to be created to get the same amount of current as the gammas of the ^{137}Cs source could produce. We have also determined that the ^{90}Sr or ^{106}Ru sources are much better for determine position resolution than the ^{137}Cs source, because the gammas produced in the ^{137}Cs decay are more penetrating than the betas produced in the ^{90}Sr decay, and therefore cannot be as collimated as the electrons. The gammas, therefore scatter through more of the outlying scintillator than the beta particles provided a less defined roll off of current versus position than the beta particles produced in ^{90}Sr .

These results will serve as a basis of comparison for Brian Wolthuis source testing of plane 0. The ^{90}Sr and ^{106}Ru sources also provides a cheaper simpler source testing setup. Since less shielding is required for the beta particles the sheet of iron need as well as the large zinc collimator can be disposed of in favor of a lighter smaller

source than can be easier to maneuver. The disadvantage of using a beta source is that since the electrons do not penetrate very far into the scintillator the energy depositions in the top and bottom scintillators would show significant differences, and the electronics used to measure the currents would have to be able to measure a wide range of currents.

These tests will be used to determine the sources used in future source testing. The ^{106}Ru source seems to be a better choice of radioactive sources for future source testing; however, the consideration of its short half life must be taken into account before the purchase is made.

References

- [1] M.C. Gonzalez-Garcia, Y. Nir, "Neutrino Masses and Mixing: Evidence and Implications," *Rev.Mod.Phys.* 75 (2003) 345-402.
- [2] S. Eidelman et al. "Particle Data Group - The Review of Particle Physics". *Physics Letters B* 592 (1). Chapter 15: Neutrino mass, mixing, and flavor change. Revised September 2005.
- [3] Nelson, J. K. "Experimental Neutrino Physics," Talk for REU, Minerva Collaboration. 2006
- [4] "Technical design report for MINER ν A detectors," The MINER ν A Collaboration, NuMI-L-703, (2006).
- [5] Adamson, P. et al, Photoelectron Counting by Several Methods, Fermilab Publications, NuMI-L-661, (August 2000).
- [6] Albayrak, Ibrahim and Eric Christy "Preliminary OD Doublet Light Yield Roll-off Tests," Hampton University, (2006).

http://www.jlab.org/~christy/Minerva/od_lytests.doc
- [7] Bellamy, E. H. et al, "Absolute Calibration and Monitoring of a Spectrometric Channel Using a Photomultiplier" *Nuclear Instruments and Methods in Physics Research A* 339 (1994) 468-476.
- [8] French, A. P. *Special Relativity*. WW Norton & Company, 1968.
- [9] Christy, Eric, Hampton University, Personal Communication.
- [10] Damiani, Dan, College of William and Mary, Personal Communication.
- [11] Flight, Robert, University of Rochester, Personal Communication.
- [12] Compton Scattering Picture

http://www.columbia.edu/cu/physics/pdf-files/Lab_2-10.pdf
- [13] the MINER ν A Collaborators The Physics Case and Proposed Detector Technologies for MINER ν A, a High Statistics Neutrino Scattering Experiment Using a Fine-grained Detector in the NuMI Beam

<http://MINERvA-docdb.fnal.gov:8080/cgi-bin/ShowDocument>
- [14] "Neutrino Oscillations" Wikipedia Collaboration. February 2007.

http://en.wikipedia.org/wiki/Neutrino_oscillation
- [15] J. K. Nelson, "The value management case for not optically coupling the OD fibers,"

<http://MINERvA-docdb.fnal.gov:8080/cgi-bin/ShowDocument?docid=1235>
- [16] M. C. Snyder, "Design of the Scintillator Counters for the MINER ν A Neutrino Detector," Thesis, College of William and Mary (2006).
- [17] ROOT Reference Guide,

<http://root.cern.ch/root/Reference.html>, April 2006.

A Monte Carlo Geometry Construction

```
//
// $Id: MapDetectorConstruction.cc Exp $
//
//authors Alberto Gago & Leonidas Aliaga (PUCP-MINERvA)
//modified by Kelly Sassin (WM-MINERvA)

#include "MapDetectorConstruction.hh"
#include "MapTrackerSD.hh"
#include "G4Material.hh"
#include "G4MaterialTable.hh"
#include "G4Box.hh"
#include "G4Trd.hh"
#include "G4LogicalVolume.hh"
#include "G4ThreeVector.hh"
#include "G4PVPlacement.hh"
#include "globals.hh"
#include "G4Cons.hh"
#include "G4Tubs.hh"
#include "G4Trap.hh"
#include "G4Sphere.hh"
#include "G4Polyhedra.hh"
#include "G4RegionStore.hh"
#include "G4Region.hh"
#include "G4UnionSolid.hh"
#include "G4RotationMatrix.hh"
#include "G4SubtractionSolid.hh"
#include "G4Element.hh"
#include "G4Colour.hh"
#include "G4VisAttributes.hh"
#include "G4SDManager.hh"
#include "MapStripParameterisation.hh"
#include "G4PVParameterised.hh"

MapDetectorConstruction::MapDetectorConstruction()
: experimentalHall_log(0),experimentalHall_phys(0),
  logicStrip(0),physiStrip(0),
  sourcetub_log(0), sourcetub_phys(0),
  sourcetubaux_log(0), sourcetubaux_phys(0),
  airsphe_log(0), airsphe_phys(0),
  octa_log(0), octa_phys(0),
  logicsemiplano(0),physisemiplano(0),steel_log(0), steel_phys(0)
{;}

MapDetectorConstruction::~MapDetectorConstruction()
{
}

G4VPhysicalVolume* MapDetectorConstruction::Construct()
{

  //----- materials

  G4double a; // atomic mass
  G4double z; // atomic number
  G4double density;
  G4int nel,natoms;
```

```

G4String symbol;

G4Material* Pb =
new G4Material("Lead", z= 82., a= 207.19*g/mole, density= 11.35*g/cm3);
G4Material* Fe =
new G4Material("Fe", z= 26., a= 55.847*g/mole, density= 7.86*g/cm3);

//-----
//Added by Kelly Sassin on April 5, 2007

G4Element* Zn =
  new G4Element("Zinc", "Zn", z= 30., a= 65.409*g/mole);

G4Element* Cu =
  new G4Element("Copper", "Cu", z= 29., a= 63.546*g/mole);

G4Material* Brass = new G4Material("Brass", density= 8.75*g/cm3, nel=2);
Brass->AddElement(Cu, 80*perCent);
Brass->AddElement(Zn, 20*perCent);

//end additions
//-----

//Air
G4Element* N = new G4Element("Nitrogen", "N", z=7., a= 14.01*g/mole);
G4Element* O = new G4Element("Oxygen" , "O", z=8., a= 16.00*g/mole);
G4Material* Air = new G4Material("Air", density= 1.29*mg/cm3, nel=2);
Air->AddElement(N, 70*perCent);
Air->AddElement(O, 30*perCent);

//Scintillator
G4Element* H = new G4Element("Hydrogen",symbol="H" , z= 1., a= 1.01*g/mole);
G4Element* C = new G4Element("Carbon" ,symbol="C" , z= 6., a= 12.01*g/mole);
G4Material* Sci = new G4Material("Scintillator", density= 1.032*g/cm3, nel=2);
Sci->AddElement(C, natoms=9);
Sci->AddElement(H, natoms=10);

//WLSFiber
G4int polyPMMA = 1;
G4int nC_PMMA = 3 + 2* polyPMMA;
G4int nH_PMMA = 6 + 2* polyPMMA;
G4Material* PMMA = new G4Material("PMMA", density=1190*kg/m3,3);
PMMA->AddElement(H,nH_PMMA);
PMMA->AddElement(C,nC_PMMA);
PMMA->AddElement(O,2);

//*****//

//-----volumes-----
//----- experimental hall (world volume)
G4double expHall_x = 2.55*m;
G4double expHall_y = 2.55*m;
G4double expHall_z = 2.55*m;
G4Box* experimentalHall_box
  = new G4Box("expHall_box",expHall_x,expHall_y,expHall_z);
experimentalHall_log = new G4LogicalVolume(experimentalHall_box,

```

```

                                Air,"expHall_log",0,0,0);
experimentalHall_phys = new G4PVPlacement(0,G4ThreeVector(),
                                experimentalHall_log,"expHall",0,false,0);
experimentalHall_log->SetVisAttributes (G4VisAttributes::Invisible);

//-----
//Modified by Kelly Sassin
//---- a cylinder for the source

G4double pr_minS = 0.0*cm;

G4double pr_maxS = 7.65*cm;

//For a collimator of radius 5.08 cm
// G4double pr_maxS = 5.08*cm;

G4double pd_zS = 2.7*cm;

//For collimator of height 2 cm
//G4double pd_zS = 2*cm;

G4double ps_phyS = 0.0;
G4double pd_phyS = 360.0*degree;
G4Tubs* tubo_source = new G4Tubs("Tubo_source",pr_minS,pr_maxS,
    pd_zS,ps_phyS,pd_phyS);
//Changed on April 5, 2007 from Fe to Zn
sourcetub_log = new G4LogicalVolume(tubo_source,Brass,"TUBO_SOURCE_log");
//sourcetub_log = new G4LogicalVolume(tubo_source,Air,"TUBO_SOURCE_log");
G4double tcsPos_xS = 0.0*cm;
G4double tcsPos_yS = 0.*m;
G4double tcsPos_zS = -1.5*cm;
sourcetub_phys = new G4PVPlacement(0,G4ThreeVector(tcsPos_xS,tcsPos_yS,tcsPos_zS),
    sourcetub_log,"TUBO_SOURCE",octa_log,false,0,false);
G4VisAttributes* pcolts=new G4VisAttributes(G4Colour(3.5,2.5,0.25));
pcolts->SetForceSolid(true);
sourcetub_log->SetVisAttributes(pcolts);

// for complete the cylinder for the source

G4double pd_zSaux = 5.2*cm;

//For collumator of height 2 cm
// G4double pd_zSaux = 2*cm;

//end modifications
//-----

G4Tubs* tubo_sourceaux = new G4Tubs("Tubo_source",pr_minS,pr_maxS,
    pd_zSaux,ps_phyS,pd_phyS);

//-----
//Modified by Kelly Sassin

sourcetubaux_log = new G4LogicalVolume(tubo_sourceaux,Brass,"TUBO_SOURCEAUX_log");
G4double tcsPos_xSaux = 0*mm;
G4double tcsPos_zSaux = -6.9075*cm;

```

```

//end modifications
//-----

sourcetubaux_phys = new G4PVPlacement(0,G4ThreeVector(tcsPos_xSaux,
  tcsPos_yS,tcsPos_zSaux),sourcetubaux_log,"TUBO_SOURCEAUX",
  experimentalHall_log,false,0,false);
G4VisAttributes* pcoltsaux=new G4VisAttributes(G4Colour(3.5,2.5,0.25));
pcoltsaux->SetForceSolid(true);
sourcetubaux_log->SetVisAttributes(pcolts);

//---- air inside tube of Fe for placing the source

//-----
//Modified by Kelly Sassin
//to change the parameters of the air inside the collumator

G4double air_minS = 0.0*cm;
G4double air_maxS = 1*cm;
G4double air_zS = 5.2*cm;

//end modifications
//-----

//G4double air_phyS = 0.0;
G4double air_phyS = 360.0*degree;
G4Tubs* air_sphe = new G4Tubs("air_sphe",air_minS,air_maxS,air_zS,air_phyS,air_phyS);
airsphe_log = new G4LogicalVolume(air_sphe,Air,"airs_sphe");
G4double tcsPos_xcyl = 0.*cm;
G4double tcsPos_ycyl = 0.*cm;
G4double tcsPos_zcyl = 0.*cm;
airsphe_phys = new G4PVPlacement(0,G4ThreeVector(tcsPos_xcyl,tcsPos_ycyl,tcsPos_zcyl),
  airsphe_log,"air_sphe",sourcetubaux_log,false,0,false);
G4VisAttributes* pcolas=new G4VisAttributes(G4Colour(3.5,2.0,1.25));
pcolas->SetForceSolid(true);
airsphe_log->SetVisAttributes(pcolas);

// Mother volume for parameterised semi-plane
G4double stripmax = 49.5/2.*cm;
G4Trd* semiplano = new G4Trd("SEMIPLANO",33/2*cm,36.3/2.*cm,
  stripmax,stripmax,1.7/2.*cm);

  logicsemiplano = new G4LogicalVolume(semiplano,//its solid
    Sci,//its material
    "SEMIPLANOBOX"); //its name
G4RotationMatrix* rot_plane = new G4RotationMatrix ;

//-----
//Added by Kelly Sassin
// G4VisAttributes* mom =new G4VisAttributes(G4Colour(1.,0.,1.));
//mom->SetForceSolid(true);
//logicsemiplano->SetVisAttributes(mom);
//end modifications
//-----

```

```

//-----
//Modified by Kelly Sassin on April 18, 2007
//Change the orientation of the plane 180 degrees so the
//strip can be read from both sides

// Here you can change the orientation of the plane
rot_plane->rotateX(180.*deg);

//end modifications
//-----
physisemiplano = new G4PVPlacement(rot_plane,//no rotation
    G4ThreeVector(0.*cm,0,0*cm),//at (0,0,0)
    logicsemiplano,//its logical volume
    "SEMIPLANOPHYSI",//its name
    experimentalHall_log,//its mother volume
    false,//no boolean operation
    0); //copy number

//-----
//Added by Kelly Sassin
//For Sr and Ru (Beta decay) sources.
//The scintillator strips are placed very close to the source so
//the source stays collimated

// physisemiplano = new G4PVPlacement(rot_plane,//no rotation
//     G4ThreeVector(0.*cm,0,-3.6*cm),//at (0,0,0)
//     logicsemiplano,//its logical volume
//     "SEMIPLANOPHYSI",//its name
//     experimentalHall_log,//its mother volume
//     false,//no boolean operation
//     0); //copy number

//end additions
//-----

//-----
// parametrized strips
//-----

solidStrip = new G4Trd("Strip",0.,1.65*cm,122.9*cm,122.9*cm,0.85*cm);
logicStrip = new G4LogicalVolume(solidStrip,Sci,"Strip",0,0,0);

//-----
//Added by Kelly Sassin
//Sequential Change in the X position of strip 1

//Center
//G4double firstposX      = 0*cm;

//4mm
//G4double firstposX      = -0.4*cm;

//8mm
// G4double firstposX     = -0.8*cm;

//12mm

```

```

//G4double firstposX      = -1.2*cm;

//17mm
//G4double firstposX      = -1.7*cm;

//21mm
// G4double firstposX     = -2.1*cm;

//25mm
//G4double firstposX     = -2.5*cm;

//33mm
// G4double firstposX     = -3.3*cm;

//49mm
//G4double firstposX     = -4.9*cm;

//65mm
// G4double firstposX     = -6.5*cm;

//For 21 strips
//16.5cm
G4double firstposX      = -16.5*cm;

//For 7 strips (center)
//G4double firstposX     = -4.95*cm;

//For 7 strips (off 1/2 strip)
//G4double firstposX     = -6.6*cm;

//end additions
//-----
G4double firstlenY      = 49.5*cm;
G4double lastlenY      = 49.5*cm;
G4double stripSpacing   = 3.3/2.*cm;

//-----
//Modified by Kelly Sassin
//Changed the number of strips that are being read out to 1
G4int NbOfStrips       = 21;
//end modifications

G4VPVParameterisation* stripParam =
new MapStripParameterisation(NbOfStrips,firstposX,stripSpacing,
firstlenY,lastlenY);
physiStrip = new G4PVPParameterised("Strip",logicStrip,
logicsemiplano,kXAxis,NbOfStrips,stripParam);

G4SDManager* SDman = G4SDManager::GetSDMpointer();
G4String trackerSDname = "/mydet/tracker";
MapTrackerSD * trackerSD = new MapTrackerSD(trackerSDname);
SDman->AddNewDetector(trackerSD);

logicStrip->SetSensitiveDetector(trackerSD);

//-----

```

```

//Modified by Kelly Sassin April 18, 2007
//Sets the scintillator color to Yellow

//G4VisAttributes* pcolostrip=new G4VisAttributes(G4Colour(1.,10.,0.));
//pcolostrip->SetForceSolid(true);
//logicStrip->SetVisAttributes(pcolostrip);

//end modifications
//-----

//-----
//added by Kelly Sassin on April 9, 2007

    G4double minimum = 0.0*cm;
    G4double maximum = 20.0*cm;
    G4double zvalue = .1*cm;
    G4double ps = 0.0;
    G4double pd = 360.0*degree;
    G4Tubs* steel = new G4Tubs("steel",minimum,maximum,zvalue,ps,pd);
    steel_log = new G4LogicalVolume(steel,Fe,"STEEL_log");
        sourcetub_log = new G4LogicalVolume(tubo_source,Air,"TUBO_SOURCE_log");
    G4double tcsPosition_xS = 0.0*cm;
    G4double tcsPosition_yS = 0.0*cm;

    G4double tcsPosition_zS = -1*cm;

//for 2 cm collumator and source
//G4double tcsPosition_zS = -4.5*cm;

    steel_phys = new G4PVPlacement(0,G4ThreeVector(tcsPosition_xS,tcsPosition_yS,
    tcsPosition_zS),steel_log,"STEEL",experimentalHall_log,false,0,false);
    G4VisAttributes* psteel=new G4VisAttributes(G4Colour(.5,.5,.5));
    psteel->SetForceSolid(true);
    steel_log->SetVisAttributes(psteel);

//end additions
//-----
return experimentalHall_phys;
}

```

B OD testing code

```
/******  
 * Project: MINERvA - WBS3  
 * Package: ROOT  
 * File: $Id: OD_data_plot_v4.C $  
 * Authors:  
 * Kelly Sassin, kesass@wm.edu  
 * Daniel Damiani, dsdami@wm.edu  
*****/  
#include <iostream>  
#include <fstream>  
#include <sstream>  
  
//ROOT specific header files  
#include "TCanvas.h"  
#include "TGraphErrors.h"  
#include "TStyle.h"  
#include "TF1.h"  
#include "TH2D.h"  
#include "TString.h"  
#include "TAxis.h"  
#include "TFrame.h"  
#include "TLegend.h"  
  
using namespace std;  
  
/* Function converts an int to a string  
 param int i - int to be converted  
 return string - string representation of int  
*/  
string intostr(int i){ //converts int to string  
    stringstream s;  
    s << i;  
    return s.str();  
} //end intstr  
  
/* Function reads in data files created by OD_test and plots them to a  
 histogram  
 param TString plotfile - location/name of a file containing the paths  
 and names of the data files to be read in by the program.  
 param bool gauss_mean - determines whether the TGraph portrayed is  
 the gaussian mean or the calculated mean  
*/  
void OD_data_plot(TString plotfile, bool gauss_mean) {  
  
    int i=0, k=0;  
    string strip_num, graph_name;  
    //Functions determining the plot of the gaussian average and  
    //calculated average and their subsequent error bars  
  
    double gauss_aver, calc_aver, gauss_error, calc_error;  
    double average[8][8], error[8][8], position[8];  
  
    TGraphErrors *curve[8];  
    //Window in which the curves will be plotted  
    TCanvas *cvmain;  
    TLegend *legend;  
    TString legend_name;
```

```

//Defines x-axis positions
position[0]=2.5;
position[1]=5;
position[2]=10;
position[3]=20;
position[4]=30;
position[5]=40;
position[6]=50;
position[7]=60;

//Reads in list of data files
// **Note** The data file names should be ordered in this file so that
//the files each individual doublet are listed together in groups of
//eight from OD_test_v*.C

ifstream ifile ((const char*) plotfile);
if ( ifile.fail() ) {
    cout << " File " << plotfile << " not found!" << endl;
    exit(0);
} else cout << " File " << plotfile << " opened." << endl;

while (ifile >> strip_num >> gauss_aver >> calc_aver >>
gauss_error >> calc_error) {
    if (k==8){
        k=0;
        i++;
    }
    \\We multiply the gaussian average by negative 1 to have both the gauss
    \\average and the calc average appear on the same graph
    if (gauss_mean) {
        average[i][k] = -1 * gauss_aver;
        error[i][k] = gauss_error;
    }
    else {
        average[i][k] = -1 * calc_aver;
        error[i][k] = calc_error;
    }
    k++;
}
ifile.close();

//Main section of program - defines the different curves that will be
put into the histogram, as well as the error bars that will appear at
each position on the x-axis

for (int j=0; j<8; j++) {
    graph_name = "OD_test_data" + intostr(j+1);
    curve[j] = new TGraphErrors(8,position,average[j],NULL,error[j]);
}

//defines the parameters of the plot
cvmain = new TCanvas("OD Test Data","OD Test Data",1024,768);
legend = new TLegend(0.58,0.7,0.88,0.88);

curve[0]->SetMarkerStyle(20);
curve[0]->SetMarkerSize(0.5);
curve[0]->SetTitle("OD LY_test Results");

```

```

curve[0]->GetXaxis()->SetTitle("Position (cm)");
curve[0]->GetYaxis()->SetTitle("Light Yield");
curve[0]->Draw("AP");
curve[0]->GetYaxis()->SetRangeUser(0,6e-11);

//adds entries into the legend
legend->AddEntry(curve[0],"No Paint, No Glue","lp");
legend->AddEntry(curve[1],"Fibers Glued, Top & End Painted","lp");
legend->AddEntry(curve[2],"Fibers Glued, Top Painted","lp");
legend->AddEntry(curve[3],"Fibers Glued, End Painted","lp");
legend->AddEntry(curve[4],"Fibers Glued","lp");
legend->AddEntry(curve[5],"Fibers Glued, Top & End Painted","lp");
legend->AddEntry(curve[6],"Fibers Glued, Top & End Painted","lp");
legend->AddEntry(curve[7],"Ends Painted, No Glue","lp");
legend->SetTextFont(72);
legend->SetTextSize(0.02);

//changes the colors of the curves so each curve appears as a different color
for (int p=1;p<8;p++) {
    curve[p]->SetMarkerStyle(20);
    curve[p]->SetMarkerSize(0.5);
    curve[p]->SetMarkerColor(p+1);
    curve[p]->SetLineColor(p+1);
    curve[p]->Draw("P");
    curve[p]->SetLineWidth(4);
}
legend->Draw();
cvmain->Update();
}

```